SEDIMENTOLOGY the journal of the International Association of Sedimentologists

Sedimentology (2023) doi: 10.1111/sed.13086

Stratigraphic change in flow transformation processes recorded in early post-rift deep-marine intraslope lobe complexes

ANDER MARTINEZ-DOÑATE*, IAN A. KANE*, DAVID M. HODGSON†, AURELIA M.-L. J. PRIVAT†, CHRISTOPHER A.-L. JACKSON‡, ERNESTO SCHWARZ§ and STEPHEN S. FLINT*

**School of Earth and Environmental Sciences, University of Manchester, Oxford Road, Manchester, M13 9PL, UK (E-mail: andermartinezdonate@gmail.com)*

†School of Earth and Environment, University of Leeds, Woodhouse, Leeds, LS2 9JT, UK

‡Department of Earth Science and Engineering, Imperial College, Prince Consort Road, London, SW7 2BP, UK

§Centro de Investigaciones Geológicas (CIG), Diag. 113 y 64, B1900, La Plata, Provincia de Buenos Aires, Argentina

Associate Editor – Victoria Valdez

ABSTRACT

The Early Jurassic Los Molles Formation in the Neuquén Basin of western Argentina is a rare example of well-exposed syn-rift to post-rift stratigraphy. In the Chachil Graben, the onset of the early post-rift stage is marked by drowning of a carbonate system and the development of two deep-marine intraslope lobe complexes. This field-based study in the Chachil Graben involved field mapping and correlating eleven stratigraphic logs, and petrographic analysis to document how grain size and texture within intraslope lobe sandstones change from the lobe centre to their frontal pinch-out. Eight different bed-scale facies are identified and inferred to be formed by turbulent (turbidites; Type A and B beds), transient turbulent–laminar (transitional flow deposits; Type C, D, E and F beds), laminar gravity flows (debrites; Type G) and post-depositional clastic injections (injectites; Type H beds). Fifteen lobes form two stacked lobe complexes that show stratigraphic evolution from a lower argillaceous sandstone-dominated lobe complex, built by transitional flow deposits, to an upper coarser-grained, sandier lobe complex largely constructed by turbidites. Petrographic analysis quantified sandstone mineralogy, matrix content, grain size and sorting, revealing that both lobe complexes are volcanic arc-sourced. This study proposes that the differences in the character of the two lobe complexes are due to maturation of sediment transport routes through progressive healing of the intraslope relief, with a concomitant decrease in substrate erosion and flow bulking. Also proposed here is a model for intraslope lobe complex development that accounts for the impact of flow-confinement on flow behaviour and transformation induced by the inherited topography. Bed type distribution suggests that high-density flows terminate more abruptly against confining slopes and produce greater depositional variability than lower-density flows. This integrated petrographic, architectural and sedimentary process model provides new insights into how post-rift intraslope lobe systems may act as hydrocarbon reservoirs, aquifers and carbon storage sites.

Keywords Confinement, depositional reservoir quality, intraslope, lobes, pinch-out, seafloor topography, transitional flow deposits.

INTRODUCTION

Submarine lobes are built from the deposits of sediment gravity flows exiting submarine channels and represent a major component of submarine fans in various tectonostratigraphic settings (Normark, 1970, 1978; Mutti & Ghibaudo, 1972; Mutti, 1977; Stow, 1985; Shanmugam & Moiola, 1988; Curray *et al.*, 2002). Therefore, submarine lobes represent a crucial record of the interplay of climate, tectonics and eustacy (Sømme *et al.*, 2009). Deep-marine lobes can form in a wide variety of basins and tectonic settings, such as during the syn-rift (e.g. Leppard & Gawthorpe, 2006; Strachan *et al.*, 2013; Henstra *et al.*, 2016; McArthur *et al.*, 2016; Cullen *et al.*, 2020) and post-rift stages of extensional basins (e.g. Haughton *et al.*, 2003; Southern *et al.*, 2017; Dodd *et al.*, 2019; Hansen *et al.*, 2021; Privat *et al.*, 2021) and in foreland basins (Sinclair, 2000; Bell *et al.*, 2018; Soutter *et al.*, 2019). Syn-rift depositional systems develop in isolated, normal fault-controlled depocentres that contain wedge-shaped packages of sediment fed by axial (i.e. fault-parallel) and transverse (i.e. fault-perpendicular) sediment supply systems (Ravnås & Steel, 1998). In contrast, post-rift depositional systems typically fill relief inherited from the preceding rift phase (Privat *et al.*, 2021), with regional thermal subsidence providing additional accommodation (e.g. Zachariah *et al.*, 2009a,b). As a result, post-rift sediment dispersal and resultant stratigraphic architecture can be highly variable and characterized by a range of stratal terminations onto intrabasinal topography (Prosser, 1993; Argent *et al.*, 2000; Gabrielsen *et al.*, 2001; Færseth & Lien, 2002; Dmitrieva *et al.*, 2018).

Sediment gravity flows interacting with topography can change both flow character (velocity, concentration) and direction (Kneller *et al.*, 1991; Al-Ja'Aidi *et al.*, 2004; Soutter *et al.*, 2021); the resultant deposits differ from those in unconfined settings, which generally have more predictable facies variability (e.g. Prélat *et al.*, 2009; Spychala *et al.*, 2017a,b). The influence of seafloor relief on bed types, facies transitions and the architecture of lobes bounded by steep slopes (>3°) has been well-documented in exhumed, highly confined settings (e.g. McCaffrey & Kneller, 2001; Sinclair & Tomasso, 2002; Patacci *et al.*, 2014; Soutter *et al.*, 2019). In contrast, there are fewer documented exhumed systems in which intraslope lobes developed above subtle slope changes (Smith, 2004; Burgreen & Graham, 2014; Spychala *et al.*, 2017a,b; Privat *et al.*, 2021). This is partially attributed to more subtle bed type changes and pinch-out terminations, which might have been under-recognized in exhumed and subsurface analogues. Petrographic analysis and bed-scale characterization can help us to understand flow transformations recorded at the event bed scale, which represents a single depositional event, and the physiographic configurations of intraslope settings. Syn-rift and post-rift lobe systems are typically deeply buried, and outcrop analogues are rarely well-preserved due to later deformation during basin inversion. Therefore, our understanding of their bed types, facies transitions and depositional architecture remains limited.

Early Jurassic strata in the Neuquén Basin (Fig. 1A) provide a rare example of an exhumed, syn-rift to post-rift sedimentary succession that is well-preserved and well-exposed. In the Chachil Graben, located in the south-west of the Neuquén Basin (Fig. 1B and C), the onset of the early-post rift stage is recorded by the drowning of a carbonate system and the subsequent development of an intraslope lobe system in the Los Molles Formation (Fig. 2; Privat *et al.*, 2021). The objectives of this paper are to: (i) characterize the bed types of the early post-rift submarine lobe complexes and their variability towards pinch-outs; (ii) document the petrography and texture of the different bed types to better understand flow processes and environments of deposition; and (iii) discuss the stratigraphic evolution of deep-marine lobes deposited in a confined post-rift intraslope setting. A spatially well-calibrated sedimentary and architectural model will improve our understanding of early post-rift intraslope lobes and potentially be used as an analogue for lobes in similar settings elsewhere.

GEOLOGICAL SETTING

The Neuquén Basin is located between 32°S and 40°S in central-western Argentina and central-eastern Chile, covering >160 000 km^2. It was bounded to the north-east by the Sierra Pintada System, to the south by the North Patagonian Massif, and to the west by the Andean magmatic arc (Fig. 1A; Legarreta & Uliana, 1996; Franzese & Spalletti, 2001). The stratigraphic record of the Neuquén Basin is characterized by Mesozoic (starting in the Late Triassic) to early Cenozoic, continental and marine siliciclastic, carbonate, evaporitic and volcanic rocks (Legarreta & Uliana, 1996; Howell *et al.*, 2005). Three tectonic phases are recognized in the development of the

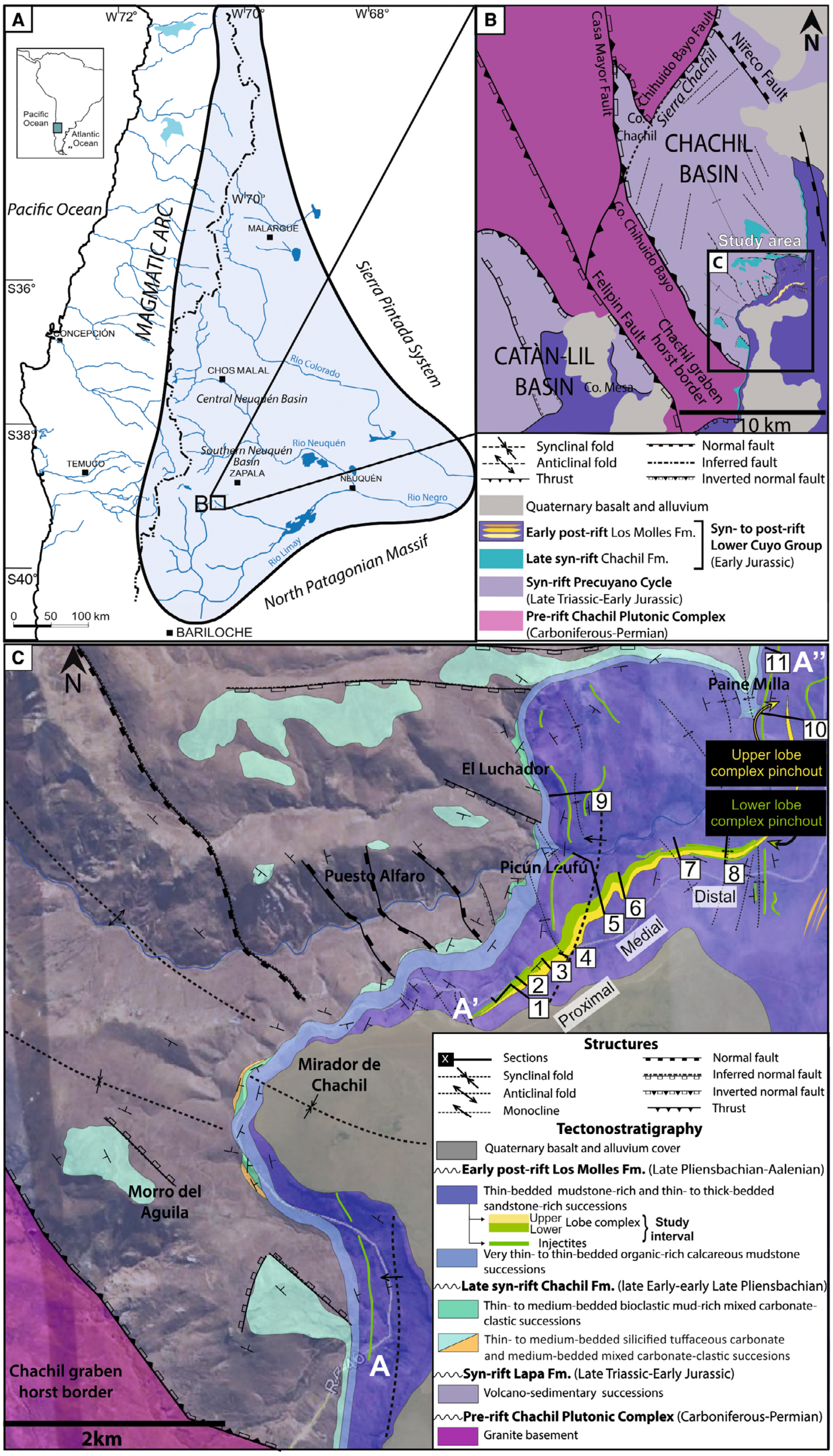

Fig. 1. (A) Location map of the Neuquén Basin (blue-shaded) and the Chachil Graben. (B) Map of the Chachil Graben (from Privat *et al.*, 2021) and detailed geological map of the study area corresponding to (C). (C) Detailed map of the Chachil Graben showing Los Molles Formation with the location of measured sections, adapted from Privat *et al.* (2021). See Fig. 2 for A–A′–A″ cross-section.

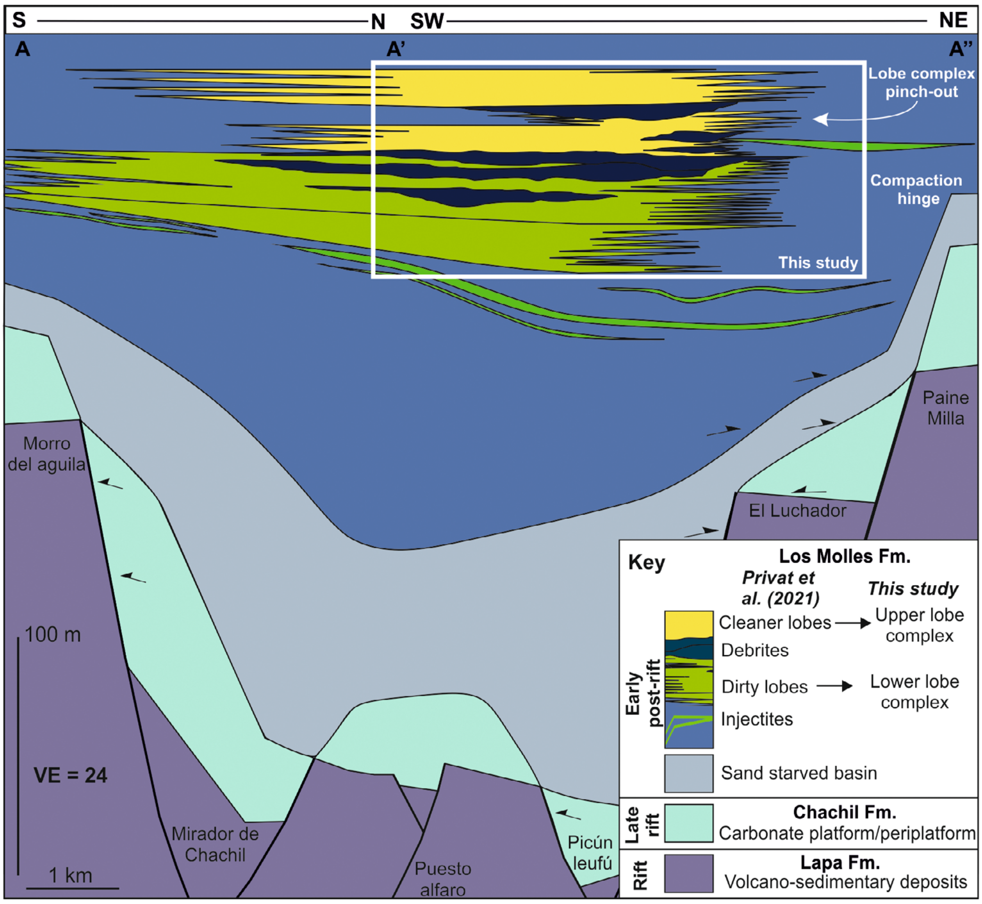

Fig. 2. Schematic correlation shows the architecture of the Lower and Upper Lobe Complexes and the debrites (modified from Privat *et al.*, 2021). The onset of the early post-rift stage is recorded by the drowning and deepening of a carbonate system and the subsequent development of a deep-water lobe system. The palaeoflow direction is towards north-east (from left to right; see rose diagrams in Fig. 13). Note that the debrites pinch out in a more proximal position than the lobe complexes, which show a progressive basinward advancement of their pinch-outs from the base to the top (more detail in Fig. 13).

Neuquén Basin (Vergani *et al.*, 1995; Franzese & Spalletti, 2001, 2003): (i) Triassic to Early Jurassic rifting, characterized by the development of narrow and isolated depocentres; (ii) Early Jurassic (Toarcian) to Early Cretaceous post-rift thermal subsidence, associated with the development of the back-arc basin; and (iii) the Late Cretaceous to early Cenozoic formation of a foreland basin related to Andean compression. This study focuses on the earliest Los Molles Formation (Toarcian; Weaver, 1931), deposited during the early post-rift stage in the Chachil Graben.

STUDY AREA: CHACHIL GRABEN

The Chachil Graben is a 15 km long, 10 km wide, NNW–SSE trending normal fault-controlled depocentre. It is bounded to the north-west and south-west by the south-east and north-west dipping Chihuido Bayo Fault system (Fig. 1B). The initial syn-rift volcano-sedimentary deposits (Lapa Formation; Precuyano Cycle) thicken northward from <400 m at the basin margins to 2 km near its centre (Franzese *et al.*, 2006). These thickness changes were controlled by fault systems striking parallel or oblique to the Chihuido Fault system along the horst forming the south-western border of the depocentre (Fig. 1B). Late syn-rift extension promoted the development of footwall highs (Paine Milla, El Luchador, Puesto Alfaro and Morro del Aguila) and lows inside the Chachil Graben (Mirador de Chachil and Picún Leufú; Figs 1C and 2; Franzese *et al.*, 2006; Privat *et al.*, 2021). Regional subsidence associated with the late syn-rift phase led to the flooding of the rift depocentres, promoting the onset of carbonate sedimentation (Chachil Formation; Weaver, 1942; Leanza *et al.*, 2013). Rapid basin deepening and drowning of the carbonate system led to the deposition of organic-rich, calcareous mudstones that draped inherited rift topography (basal Los Molles Formation; Fig. 2; Privat *et al.*, 2021). Healing of rift topography and the onset of extra-basinal siliciclastic supply promoted the development of early post-rift intraslope lobe complexes (Privat *et al.*, 2021).

Differential compaction of organic-rich mudstones over inherited rift topography promoted a long-lived seabed relief in the Chachil Graben (Fig. 2; Privat *et al.*, 2021). Similar differential compaction has also been documented in the subsurface (Cristallini *et al.*, 2009) and exhumed depocentres elsewhere in the Neuquén Basin (Veiga *et al.*, 2013). In the Chachil Graben, a south-dipping compaction hinge over the El Luchador fault block acted as an oblique counterslope to the north-east-directed sediment gravity flows, controlling the architecture and pinchout location of two submarine lobe complexes (Fig. 2; dirty and cleaner lobe complexes, *sensu* Privat *et al.*, 2021). Both lobe complexes are 6 to 8 km long, 5 km wide and <50 m thick and are bound at their base and top by a >4 m thick mudstone interval or an erosionally-based debrite (Figs 1C and 2; Privat *et al.*, 2021). This study refers to them as the Lower and Upper Lobe Complex, respectively (Fig. 2). Their constituent bed types (Fig. 3) and stratigraphic architecture are described and compared to propose an overall depositional model.

DATA AND METHODS

The dataset comprises 11 sedimentological logs 1 : 25 scale (Fig. 1C), collected over a horizontal distance of 4 km. Logs were correlated, and the overall depositional architecture was constrained by walking out individual sandstone-rich packages and several stratigraphically distinct marker beds. Data collected included lithology, bed thickness and contacts, sedimentary structures, and palaeocurrent measurements from grooves, flutes, cross-bedding, flame structures and ripple cross-lamination. Uncrewed Aerial Vehicle (UAV) photogrammetry was used in conjunction with mapping and logging to capture the architecture of the sandstone and mudstone packages within the investigated stratigraphic interval.

Petrographic analysis was performed on 40 orientated and polished thin sections collected in 16 sandstone beds logged at a 1 : 2 scale (Figs 4, 5, 6, 7, 8 and 9). To understand the longitudinal character of flows, up to five samples were taken from the base to the top of the sandstone beds (see similar methods in Kane *et al.*, 2017; Southern *et al.*, 2017; Bell *et al.*, 2018; Fildani *et al.*, 2018). The long axes of 200 grains per thin section were measured (see Table S2), enabling quantification and analysis of sorting (Folk & Ward, 1957; F & W method). Detrital components were quantified using the Gazzi-Dickinson point counting method (Gazzi, 1966; Dickinson, 1970; Zuffa, 1985). Percentage abundance was quantified by counting 400 points per thin section using an automated and motorized stepping stage controlled by PETROG software (PETROG System, Conwy Valley Systems Limited, UK). The points were stochastically distributed across an aleatory grid, where the minimum interpoint distance was larger than the coarsest grain fraction to avoid repetition (Van der Plas & Tobi, 1965). Point counting enabled the classifications of grains into 11 classes, matrix (particulate matter <0.062 mm) and cement. The results were plotted on a matrix versus mean size grain diagram (Fig. 10) and three ternary diagrams (Fig. 11; Qm–F–Lt, Dickinson, 1983; Lm–Lv–Ls, Ingersoll & Suczek, 1979; Qp–Lv–Lsm diagram, Dickinson, 1985) because combinations of specific end-members discriminate between different grain properties (Hulka & Heubeck, 2010; Ciccioli *et al.*, 2014).

BED TYPES

The sandstone beds were divided into eight bed types (Fig. 3; Type A–H beds) based on their thickness, texture (for example, matrix content, grading, mudstone clast content), grading and sedimentary structures. Petrographic analysis was used to quantify the mineralogy, matrix content, grain-size range and sorting (Type A–F beds; Figs 4, 5, 6, 7, 8 and 9) to support the outcrop-based interpretation. Samples with >15% matrix content were considered matrix-rich, while those with <15% were considered matrix-poor, based on the threshold of Pettijohn *et al.* (1972), which is similar to the one proposed in Sylvester & Lowe (2004; *ca* 16%). The authors did not differentiate between detrital and authigenic matrix, but the abundance of carbonaceous matter, micas, fine quartz and feldspar grains suggest that the matrix is predominantly detrital (Lowe & Guy, 2000). The deformation of weak detrital grains such as sedimentary lithoclasts (Ls) and

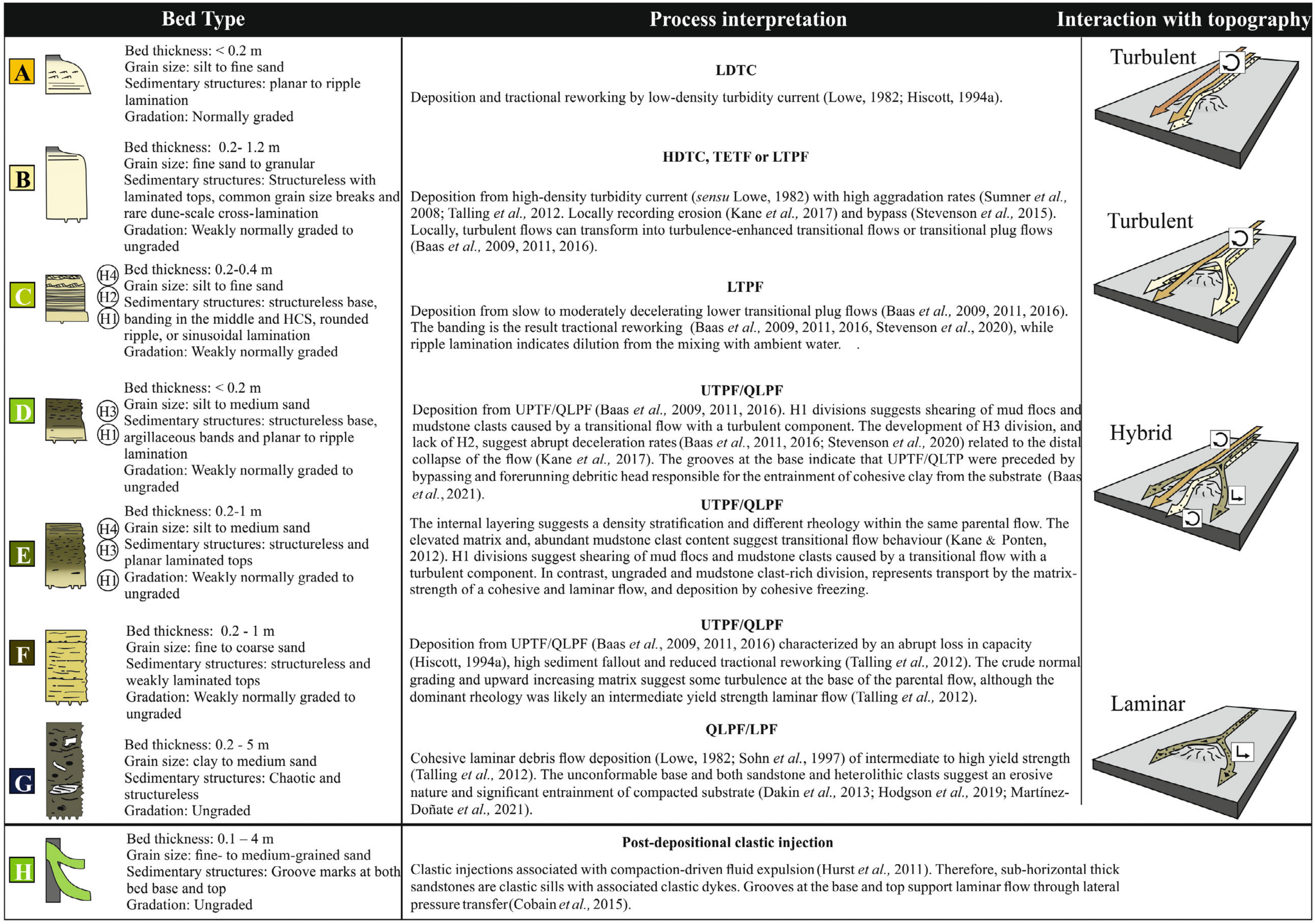

Fig. 3. Bed type descriptions, depositional process interpretations and the generalized relationship between flow rheology and the interaction with topography (from Bakke *et al.*, 2013 and modified from Al-Ja'Aidi *et al.*, 2004).

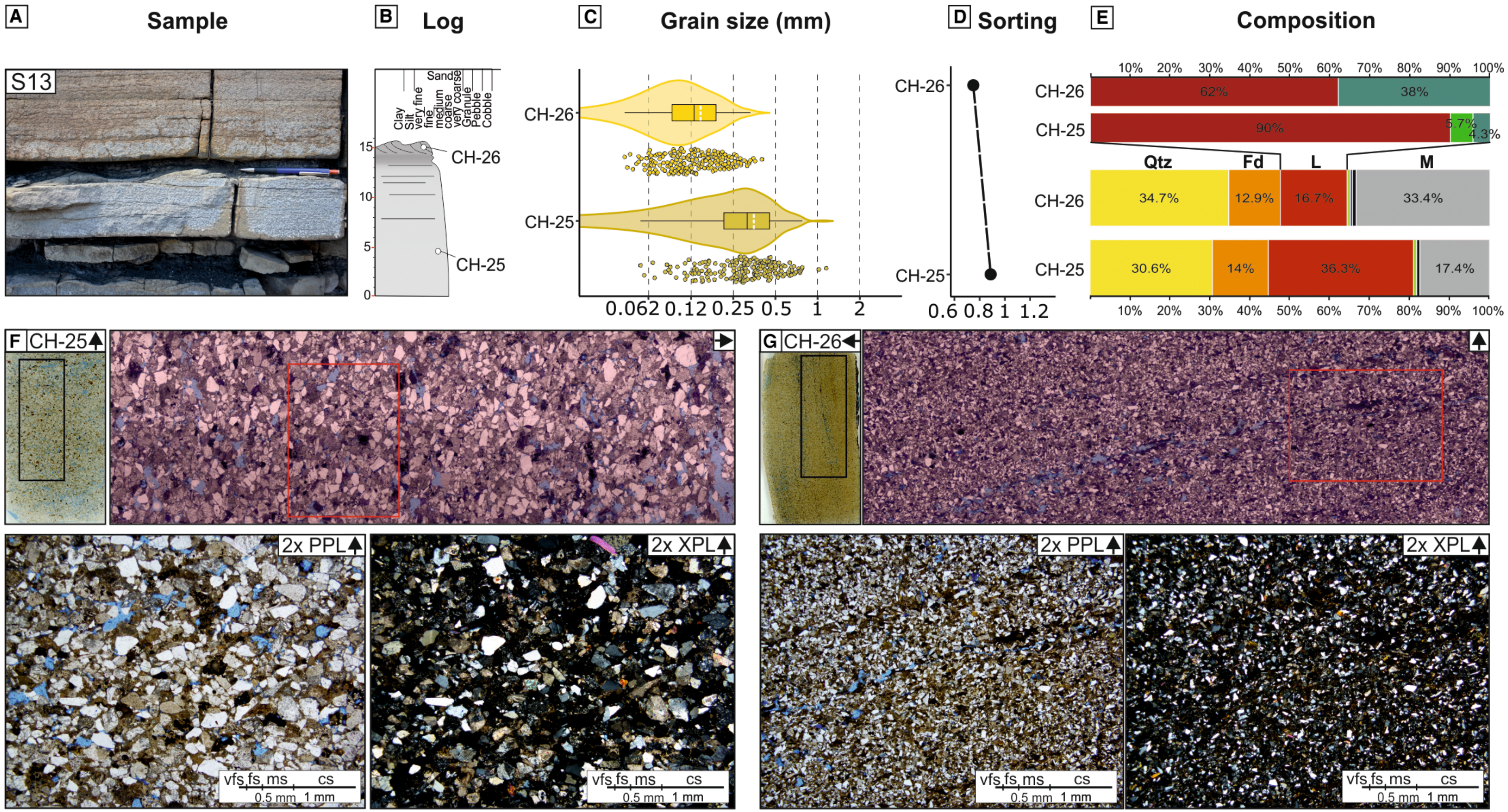

Fig. 4. Summary diagrams illustrating Type A beds, (A) outcrop photograph (13 cm long pencil for scale) and (B) detailed log (1 : 2 scale) of the sample bed, (C) grain size, (D) sorting (F & W) and (E) mineralogy; yellow (Qtz; Quartz;), orange (Fd; Feldspar), red (L; Lithoclasts) light green (sheet silicates), purple (accessory minerals), black (organic matter) grey (M; Matrix). Lithoclasts (L) are subdivided into: red (Lv: volcanic lithoclasts), green (Lm; metamorphic lithoclasts) and dark green (Ls; sedimentary lithoclasts). Representative thin section (F; CH-25 and G; CH-26) scans, photomosaic and photomicrographs (plane polarized light and cross-polarized light – PPL and XPL). Note that black squares indicate the location of the photomosaic, and red squares in the photomosaic indicate the position of the photomicrographs. The arrows in the top right show the top of the samples.

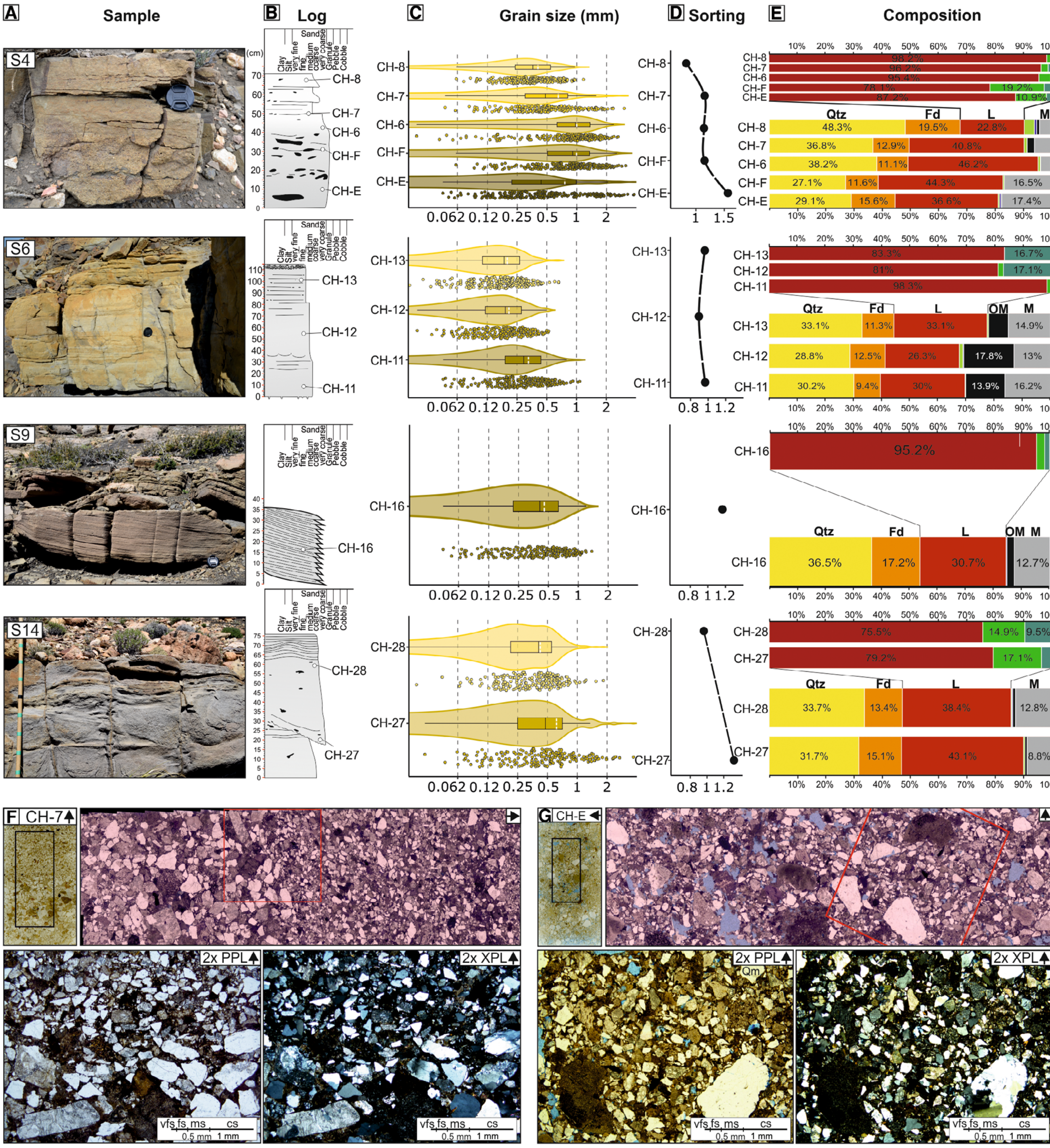

Fig. 5. Summary diagrams illustrating Type B beds, (A) outcrop photograph (6 cm diameter lens cap and 90 cm long pole for scale) and (B) detailed log (1 : 2 scale) of the sample bed, (C) grain size, (D) sorting (F & W) and (E) mineralogy; yellow (Qtz; Quartz;), orange (Fd; Feldspar), red (L; Lithoclasts) light green (sheet silicates), purple (accessory minerals), black (organic matter) grey (M; Matrix). Lithoclasts (L) are subdivided into: red (Lv; volcanic lithoclasts), green (Lm; metamorphic lithoclasts) and dark green (Ls; sedimentary lithoclasts). Representative thin section (F; CH-7 and G; CH-E) scans, photomosaic and photomicrographs (plane polarized light and cross-polarized light – PPL and XPL). Note that black squares indicate the location of the photomosaic, and red squares in the photomosaic indicate the position of the photomicrographs. The arrows in the top right show the top of the samples.

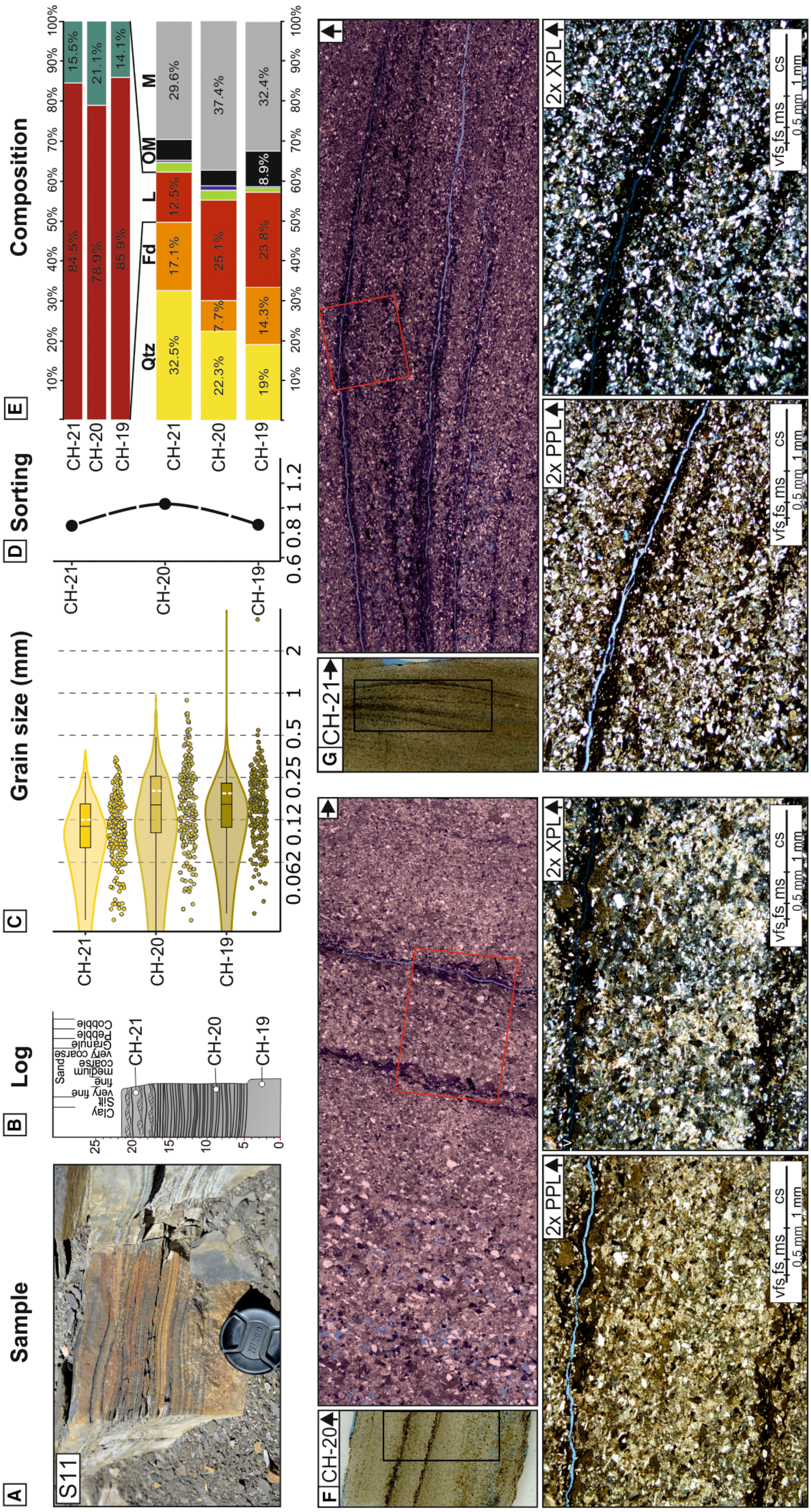

Fig. 6. Summary diagrams illustrating Type C beds, (A) outcrop photograph (6 cm diameter lens cap for scale) and (B) detailed log (1 : 2 scale) of the sample bed, (C) grain size, (D) sorting (F & W) and (E) mineralogy; yellow (Qtz; Quartz;), orange (Fd; Feldspar), red (L; Lithoclasts) light green (sheet silicates), purple (accessory minerals), black (organic matter) grey (M; Matrix). Lithoclasts (L) are subdivided into: red (Lv; volcanic lithoclasts), green (Lm; metamorphic lithoclasts) and dark green (Ls; sedimentary lithoclasts). Representative thin section (F; CH-20 and G; CH-21) scans, photomosaic and photomicrographs (plane polarized light and cross-polarized light – PPL and XPL). Note that black squares indicate the location of the photomosaic, and red squares in the photomosaic indicate the position of the photomicrographs. The arrows in the top right show the top of the samples.

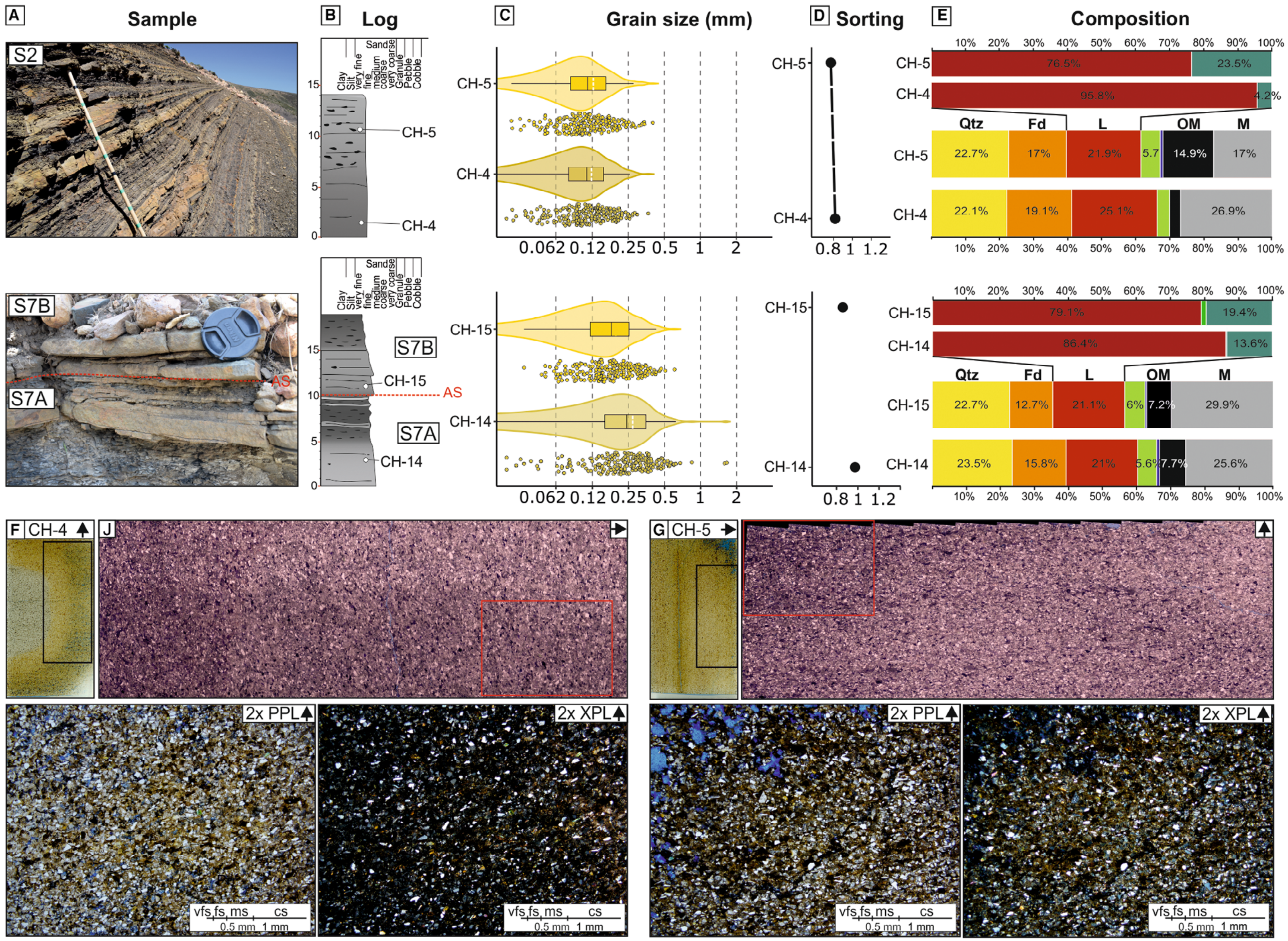

Fig. 7. Summary diagrams illustrating Type D beds, (A) outcrop photograph (6 cm diameter lens cap and 90 cm long pole for scale) and (B) detailed log (1 : 2 scale) of the sample bed, (C) grain size, (D) sorting (F & W) and (E) mineralogy; yellow (Qtz; Quartz;), orange (Fd; Feldspar), red (L; Lithoclasts) light green (sheet silicates), purple (accessory minerals), black (organic matter) grey (M; Matrix). Lithoclasts (L) are subdivided into: red (Lv; volcanic lithoclasts), green (Lm; metamorphic lithoclasts) and dark green (Ls; sedimentary lithoclasts). Representative thin section (F; CH-4 and G; CH-5) scans, photomosaic and photomicrographs (plane polarized light and cross-polarized light – PPL and XPL). Note that black squares indicate the location of the photomosaic, and red squares in the photomosaic indicate the position of the photomicrographs. The arrows in the top right show the top of the samples.

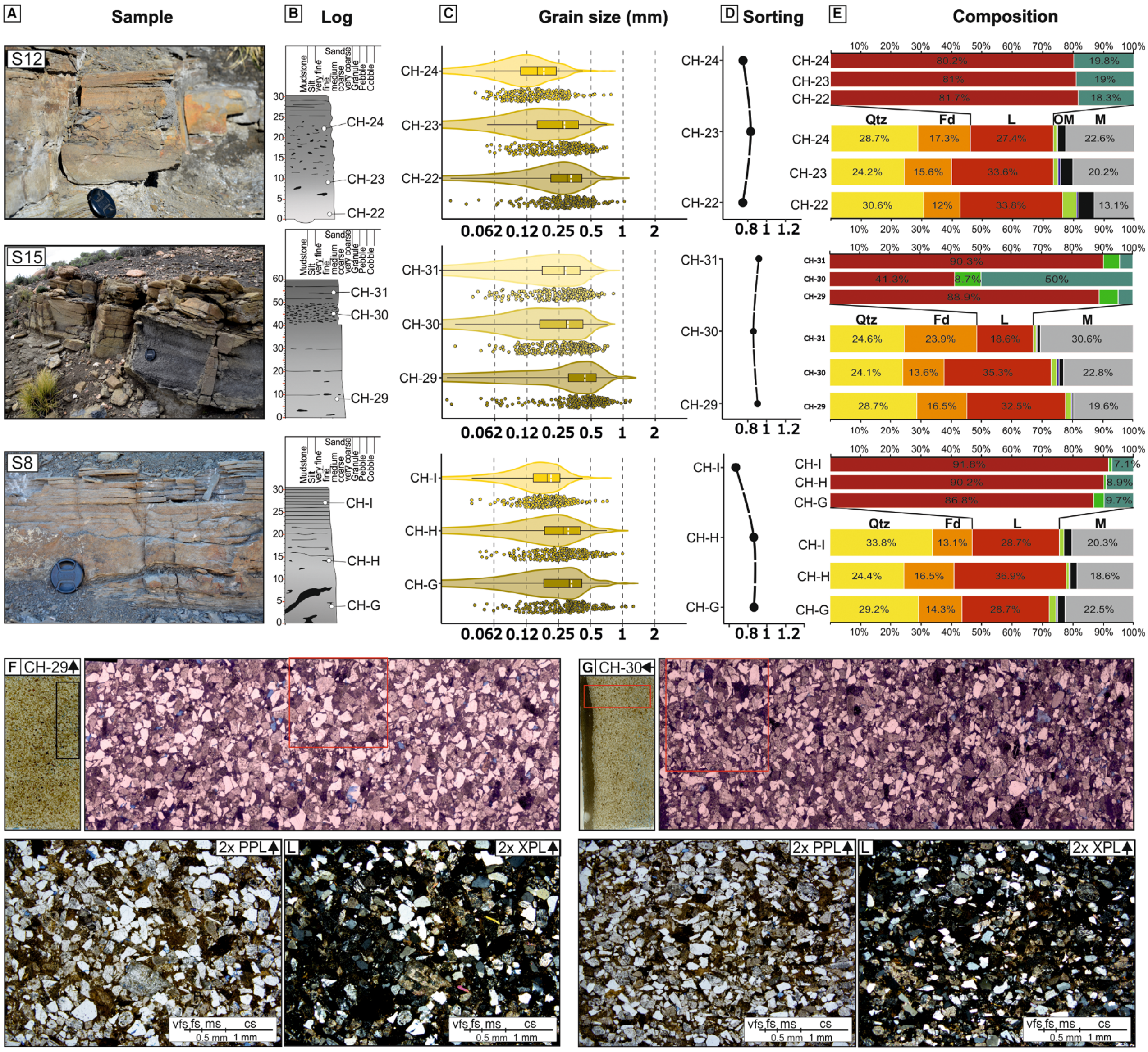

Fig. 8. Summary diagrams illustrating Type E beds, (A) outcrop photograph (6 cm diameter lens cap for scale) and (B) detailed log (1 : 2 scale) of the sample bed, (C) grain size, (D) sorting (F & W) and (E) mineralogy; yellow (Qtz; Quartz;), orange (Fd; Feldspar), red (L; Lithoclasts) light green (sheet silicates), purple (accessory minerals), black (organic matter) grey (M; Matrix). Lithoclasts (L) are subdivided into: red (Lv; volcanic lithoclasts), green (Lm; metamorphic lithoclasts) and dark green (Ls; sedimentary lithoclasts). Representative thin section (F; CH-29 and G; CH-30) scans, photomosaic and photomicrographs (plane polarized light and cross-polarized light – PPL and XPL). Note that black squares indicate the location of the photomosaic, and red squares in the photomosaic indicate the position of the photomicrographs. The arrows in the top right show the top of the samples.

devitrified volcanic clasts (Lv) contributed to the formation of the detrital matrix (pseudomatrix; Dickinson, 1970). Two additional bed types had no petrographic analysis because they were not genetically related to the flows responsible for the formation of intraslope lobes (Type G beds) or do not represent depositional event beds (Type H beds; Fig. 3).

Type A beds

Description: Thin-bedded (<0.2 m thick), matrix-rich (>15%), planar-laminated and ripple-laminated with sharp, planar bed bases and tops. Matrix content increases upward within the bed (Fig. 4; S13 sample bed: 17 to 33%). Beds are poorly to moderately well-sorted and normally

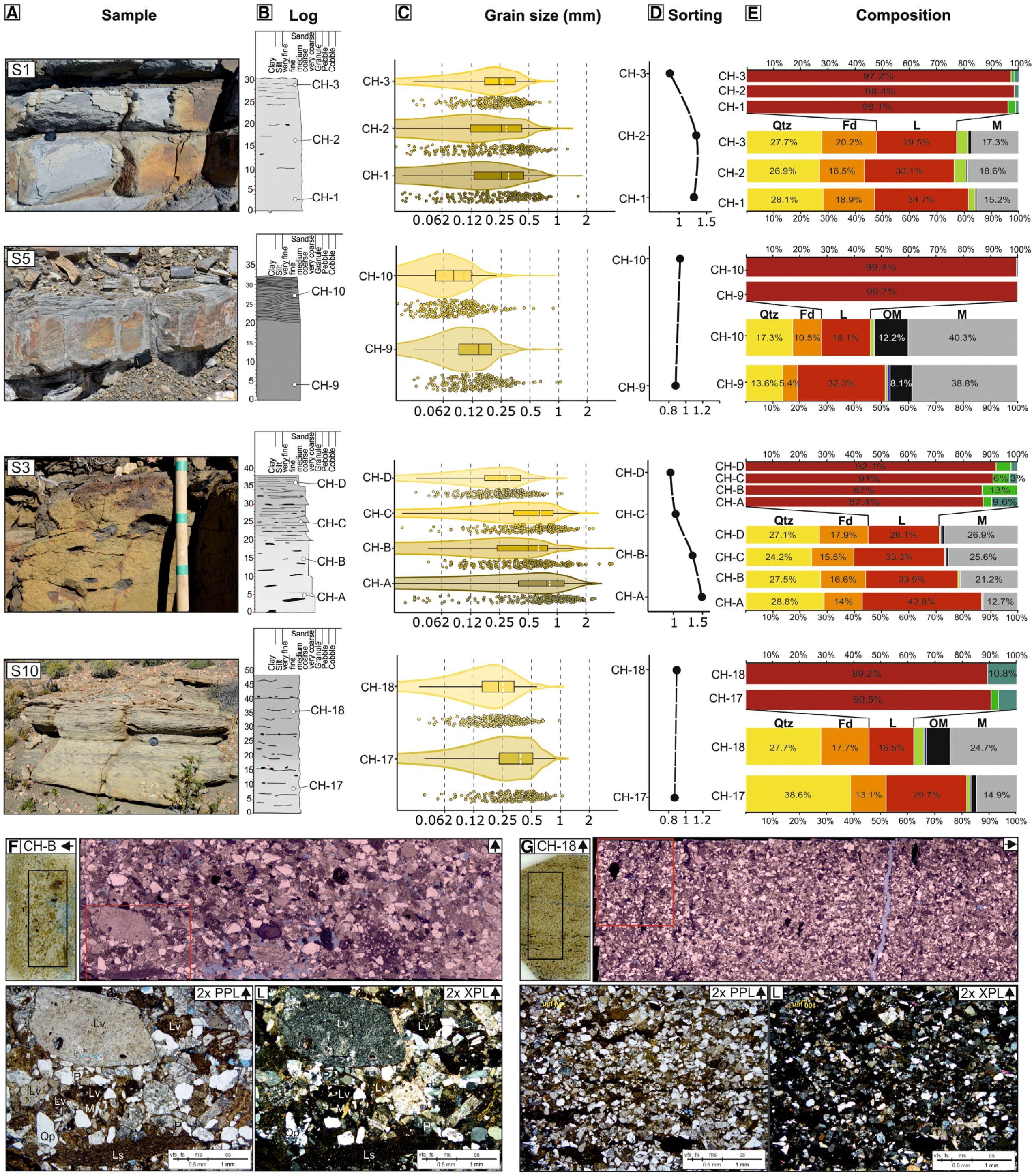

Fig. 9. Summary diagrams illustrating Type F beds, (A) outcrop photograph (6 cm diameter lens cap for scale, 10 cm long compass and 30 cm long pole for scale) and (B) detailed log (1 : 2 scale) of the sample bed, (C) grain size, (D) sorting (F & W) and (E) mineralogy; yellow (Qtz; Quartz;), orange (Fd; Feldspar), red (L; Lithoclasts) light green (sheet silicates), purple (accessory minerals), black (organic matter) grey (M; Matrix). Lithoclasts (L) are subdivided into: red (Lv; volcanic lithoclasts), green (Lm; metamorphic lithoclasts) and dark green (Ls; sedimentary lithoclasts). Representative thin section (F; CH-B and G; CH-18) scans, photomosaic and photomicrographs (plane polarized light and cross-polarized light – PPL and XPL). Note that black squares indicate the location of the photomosaic, and red squares in the photomosaic indicate the position of the photomicrographs. The arrows in the top right show the top of the samples.

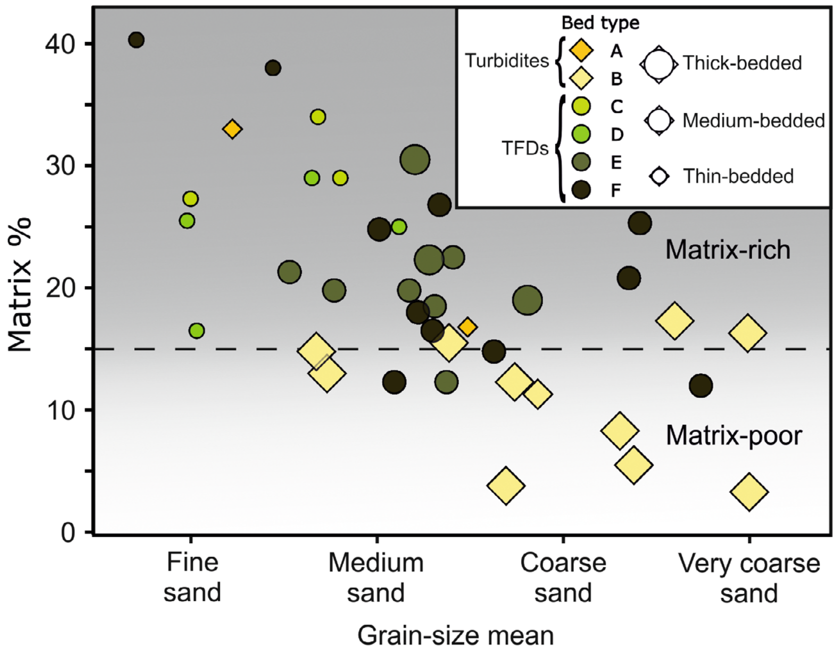

Fig. 10. Graph showing matrix content as a function of the mean grain size of each sample (n = 40) according to the bed type. The dashed line at the 15% matrix represents the threshold for matrix-poor and matrix-rich intervals (Pettijohn *et al.*, 1972). Note that the high-density turbidites (Type B beds) are the coarsest and less argillaceous, in contrast to most transitional flow deposits (Type C, D, E and F beds) and low-density turbidites (Type A bed).

graded, comprising very fine to medium-grained sandstones. When analysed under the microscope, millimetre-scale mud chips are aligned along the laminae (Fig. 4G; CH-26). Ripples suggest an overall NNE palaeocurrent. However, ripples show a broad divergence, even developing bidirectional ripple laminations. Near the pinch-outs, ripples are commonly replaced by convolute lamination.

Interpretation: These bed types represent deposition from low-density turbidites (*sensu* Lowe, 1982). Grains are suspended due to flow turbulence and deposited under aggradation rates that are sufficiently slow to permit differential grain-size settling and tractional reworking (Best & Bridge, 1992; Hiscott, 1994a; Sumner *et al.*, 2008). Bidirectional ripple laminations suggest flow deflection and reflection against seafloor relief (Kneller *et al.*, 1991; Edwards *et al.*, 1994). Convolute lamination suggests high sedimentation rates and has been attributed to the development of reflected bores and internal waves, which might be related to interaction with seafloor relief (Tinterri *et al.*, 2016). The upward increase in matrix content reflects the differential grain-size settling from waning flows, which deposits coarser material near bed bases and finer material near bed tops (Mulder & Alexander, 2001).

Type B beds

Description: Medium to thick-bedded (0.3 to 1.2 m thick), matrix-poor (<15%) sandstones, with sharp planar tops and sharp erosive bed bases with abundant multidirectional grooves with a ENE–WSW oriented dominant trend. Type B beds are moderately sorted and weakly normally graded, passing upward from coarse-grained (locally very coarse and granular) to medium to fine-grained sandstone (Fig. 5; S6 sample bed). Overall, they show an upward decrease in centimetre-scale mudstone clast and matrix content (Fig. 5; S4 sample bed: 17 to 4%), although subtle upward increasing trends are also documented (Fig. 5; S14 sample bed: 9 to 13%). Locally, some beds show subtle inverse grading ($T_{B\text{-}3}$ of Talling *et al.*, 2012) and grain-size breaks (coarse to medium-grained), associated with a decrease in matrix content (Fig. 5; S4 sample bed: 17 to 4%). Type B beds can be structureless and ungraded and contain weakly developed planar laminations (Fig. 5; S6 sample bed). However, when these bed types overlie a scour, sigmoidal north-east-dipping cross-stratifications are developed (Fig. 5; S9 sample bed; see Arnott & Al-Mufti, 2017).

Interpretation: These sandstones were deposited from erosive high-concentration flows where particles are suspended by grain-to-grain interactions and fluid turbulence (Kuenen, 1951; Middleton & Hampton, 1973). Therefore, they are interpreted as high-density turbidites (*sensu* Lowe, 1982) deposited incrementally (Kneller & Branney, 1995) under aggradation rates high enough to suppress tractional reworking

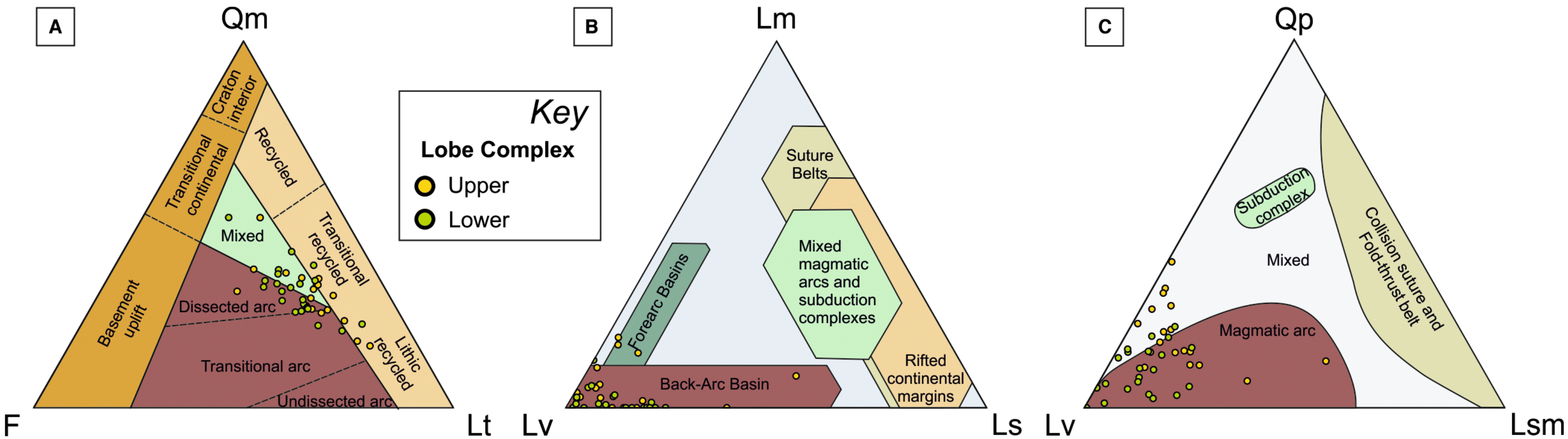

Fig. 11. Ternary diagrams of the 40 analysed samples: (A) monocrystalline quartz–feldspar–lithoclasts (Qm–F–Lt; Dickinson *et al*., 1983) show a mixed and arc provenance; (B) volcanic–metamorphic–sedimentary lithoclasts (Lv–Lm–Ls; Ingersoll & Suczek, 1979) show a volcanic arc source of the samples due to the dominance of volcanic lithoclasts (Lv) over sedimentary (Ls) and metamorphic (Lm) lithoclasts. (C) polycrystalline quartz–volcanic lithoclasts–sedimentary and metamorphic lithoclasts (Qp–Lv–Lsm; Dickinson, 1985) showing volcanic arc source.

(Lowe, 1982; Sumner *et al.*, 2008). The tractional structures and normal grading observed at bed tops indicate differential grain settling and effective shearing from waning gravity flows (Sumner *et al.*, 2008; Talling *et al.*, 2012; Terlaky & Arnott, 2014). High-angle cross-bedding developed over scours supports scour-fill rather than dune formation (see pseudo-dunes of Arnott & Al-Mufti, 2017, and references therein). Inverse grading in the lower division (for example, S4 sample bed) represents deposition under traction carpets (Lowe, 1982; Hiscott, 1994b; Sohn, 1997). The upward increase in matrix content reflects differential grain-size settling from waning flows, which deposit coarser material near the bed base and finer material near the bed top (Fig. 5; S6 and S14 sample beds; Mulder & Alexander, 2001). The high sediment fallout rate can prevent the segregation of flocs from returning into suspension, resulting in enhanced trapping of clay flocs at the flow and bed base (e.g. Middleton & Neal, 1989). Sand-sized mudstone clasts in intermediate positions within the sandstone beds suggest that either they remained in suspension for longer than particles of a similar size and density (for example, quartz and feldspar grains; Mulder & Alexander, 2001) or that they were entrained and deposited later in the lifespan of the flow. In contrast, deposits with an upward decrease in matrix content are associated with developing a cohesive viscous near-bed sublayer (near-bed laminar plug; Lowe & Guy, 2000). Grain-size breaks (Fig. 5; S4 sample bed) suggest that flow stratification developed between the cohesive viscous layer and the overlying turbulent flow division (Lowe & Guy, 2000). The grooves represent tool-like clasts that gouged the substrate (Peakall *et al.*, 2020) and indicate high-concentration flows. Groove development might be linked to the passage of a forerunning, fast-moving and bypassing debritic head, responsible for rafting mudstone clasts and transferring them as bedload, developing grooves (Baas *et al.*, 2021). Disaggregation of mudstone clasts could trigger the development of turbulence-enhanced transitional flows or even lower transitional plug flows (LTPFs; Baas *et al.*, 2009, 2011, 2016) over short distances.

Type C beds

Description: Medium-bedded (0.2 to 0.4 m), matrix-rich (>15%) sandstones, forming tripartite deposits with sharp boundaries between constituent divisions (Fig. 6; S11 sample bed). Bed bases are sharp and conformable and contain abundant ENE–WSW-oriented discontinuous tool marks (skim marks) with high divergence. The lower division of Type C beds (5 to 20 cm thick) is structureless, weakly normally graded, moderately sorted and matrix-rich (27%). The middle division (10 to 15 cm thick) is ungraded and poorly sorted, with the highest matrix content of the three divisions (37%), and characterized by low-amplitude, undulating microbanding (<1 cm spacing; Stevenson *et al.*, 2020), with alternating planar sub-parallel to undulatory, light (i.e. mud-poor) and dark (i.e. mud-rich) bands containing rare, millimetre-scale mud chips (Fig. 6F; S11 sample bed). The dark argillaceous bands are responsible for the poor sorting within this division (Fig. 6). The upper division (<5 cm thick) is normally graded matrix-rich (30%) and moderately sorted. NNE-oriented ripple lamination is common, with millimetre-scale mud chips aligned within the ripple laminae (Fig. 6).

Interpretation: Due to its similar matrix content and lack of bounding fine-grained interval, the development of the three divisions is interpreted as being deposited from the same transitional flow. The normally graded lower division suggests deposition from a flow comprising a turbulent component to permit differential grain-size settling (Lowe, 1982). The lack of tractional structures and high matrix content suggest deposition from transitional flows under moderate to high aggradation rates. The banding in the intermediate division results from deposition and reworking from transitional flows, with a sustained traction period formed within the upper-stage plane bed flow regime (Baas *et al.*, 2009, 2016; Stevenson *et al.*, 2020). Alternatively, the banding can represent episodic near-bed turbulence suppression (Lowe & Guy, 2000). Lower structureless and intermediate banded divisions suggest deposition from LTPFs (*sensu* Baas *et al.*, 2009), where mixing with ambient water developed the ripple-bearing upper division. However, the basal skim marks suggest that a bypassing laminar and concentrated head could have preceded the LTPFs because of the incompatibility between the skim marks and the turbulence state (Peakall *et al.*, 2020; Baas *et al.*, 2021). This tripartite structure is comparable to the H1 (lower division), H2 (intermediate division) and H4 (upper division) described in Haughton *et al.* (2009; Fig. 3). The lack of the linked debrite division (H3) suggests that the flows were able to deliver sand in a basinward direction (flow efficiency, *sensu* Mutti, 1979), and that they neither decelerated rapidly nor were very cohesive (Stevenson *et al.*, 2020). The divergence between the tool marks (ENE–WSW) and the ripples (NNE) suggests the existence of seabed relief where the forerunning bypassing head was more influenced by seabed relief than the more dilute depositional part of the flow, although it could be related to two different flows (Peakall *et al.*, 2020).

Type D beds

Description: Thin-bedded (<0.2 m thick), matrix-rich (>15%) sandstone, forming bipartite deposits, with sharp boundaries between its constituent divisions (Fig. 7; S2, S7A and S7B sample beds). The lower divisions (<0.2 m thick) are matrix-rich (26 to 30%), structureless, fine- to medium-grained, weakly normally graded and moderately sorted (Fig. 7), and grooves with a wide range of directions. The upper divisions (*ca* 0.1 m thick) are massive and characterized by argillaceous sandstone comprising abundant mudstone clasts and plant fragments (0.5 to 2.0 cm in length; Fig. 7). Upper divisions lack thin section observation due to the fissile character of the argillaceous sandstones.

Interpretation: The juxtaposition of the lower and upper divisions without an intervening mudstone layer suggests that they represent the H1 and H3 divisions of hybrid event beds (HEBs; see Haughton *et al.*, 2009; Fig. 3) genetically related to a single depositional event. The internal layering reflects discrete rheological changes within the source flow due to deceleration related to lateral spreading and/or increased near-bed flow concentration or cohesion (Kane *et al.*, 2017). However, the lack of abrupt boundaries suggests that the flow did not develop stable internal stratification (Kane *et al.*, 2017). The high matrix content (26 to 30%) and the crude normal grading within the lower divisions (H1) suggest the shearing of mud flocs and mudstone clasts caused by a transitional flow with a turbulent component. The upper argillaceous divisions (H3) suggest deposition from intermediate to high-yield strength debris-flow divisions (Talling *et al.*, 2012). The preservation of plant fragments supports the interpretation of a laminar state within the upper divisions (e.g. Hodgson, 2009; D2 Type). Therefore, Type D beds are interpreted as thin-bedded HEBs formed under upper transitional plug flows (UTPF) and quasi-laminar plug flows (QLPF; *sensu* Baas *et al.*, 2009, 2011, 2016). The development of H3 division, and lack of H2, suggest abrupt deceleration rates (Baas *et al.*, 2011, 2016; Stevenson *et al.*, 2020) related to the distal collapse of the flow (Kane *et al.*, 2017). The grooves at the base indicate that UPTF/QLPFs were preceded by bypassing a forerunning debritic head responsible for incorporating cohesive clay from the substrate (Baas *et al.*, 2021).

Type E beds

Description: Medium to thick-bedded (0.2 to 1.0 m thick), matrix-rich (>15%), tripartite beds with sharp and loaded bases containing abundant multidirectional grooves and sharp tops (Fig. 8). The contacts between each division are gradual (Fig. 8; S12 and S15 sample beds), and lower and intermediate divisions are structureless with abundant mudstone clasts. The lower divisions (10 to 40 cm thick) are medium-grained, matrix-rich (20 to 23%; Fig. 8; S15 and S8 sample beds) or matrix-poor (13%; Fig. 8; S12 sample bed), weakly normally graded, moderately sorted, and contain few deformed mudstone clasts (5 to 50 cm diameter; Fig. 8). The intermediate division (10 to 20 cm thick) is medium-grained, matrix-rich (19 to 23%), weakly normally graded and moderately sorted, and contains abundant, rounded mudstone clasts (0.1 to 5.0 cm diameter; Fig. 8). The uppermost division (5 to 15 cm thick) is fine-grained, matrix-rich (20 to 31%), normally graded, moderately sorted and structureless to weakly planar laminated, containing rare mudstone clasts (Fig. 8).

Interpretation: The internal layering suggests different rheologies related to HEB development (e.g. Lowe & Guy, 2000; Haughton *et al.*, 2003, 2009; Talling *et al.*, 2004; Barker *et al.*, 2008; Kane & Pontén, 2012). The lack of abrupt boundaries suggests that the flow did not develop stable internal stratification (Kane *et al.*, 2017). Loaded bases and mudstone rafts suggest shearing and entrainment of semi-consolidated substrate material and transported in suspension by flow-turbulence (see undersaturated flows of Eggenhuisen *et al.*, 2017; Kane *et al.*, 2017). The incorporation of clay-rich material and increased flow concentration promoted transitional flow behaviour (Kane & Pontén, 2012). Normal grading within the lower division (H1) suggests that the basal layer was fluid and turbulent enough to allow particle settling of the denser/coarser-grained fraction according to grain size/density (Baas *et al.*, 2009) or a low yield strength basal division (Kane *et al.*, 2017). Therefore, these matrix-rich basal divisions are not comparable to the clean sandstone turbidite base of HEBs in other systems (Haughton *et al.*, 2003, 2009; Talling *et al.*, 2004; Amy *et al.*, 2006; Barker *et al.*, 2008; Davis *et al.*, 2009) suggesting a different style of flow transformation. The abundant grooves indicate that these flows were preceded by a highly erosive bypassing debris flow and later infilled by the deposition of H1. The weakly normally graded, matrix-rich and mudstone clast-rich intermediate divisions (H3) suggest hindered settling as a sediment transport mechanism (Mulder & Alexander, 2001) and capacity-driven deposition (Hiscott, 1994a) rather than transport as a result of the matrix-strength of a high yield strength debris-flow division and cohesive freezing (Talling *et al.*, 2012). The poorly-developed lamination on the upper divisions (H4) suggests high aggradation rates with poorly developed tractional reworking on the upper-stage plane bed. Alternatively, they may be related to deposition from parts of the flow that did not incorporate enough substrate and develop a poorly debritic division (Hussain *et al.*, 2020; Baas *et al.*, 2021), such as the tail. Additionally, they can be caused by mixing ambient water (Marr *et al.*, 2001; Talling *et al.*, 2002; Sequeiros, 2012). Therefore, Type E beds are interpreted here as thick-bedded HEBs (e.g. Kane *et al.*, 2017) deposited from UTPF to QLPFs under high deceleration rates (Baas *et al.*, 2009, 2011, 2016).

Type F beds

Description: Medium to thick-bedded (0.3 to 1.0 m thick) and generally matrix-rich (>15%) sandstones. The matrix content increases upward within a bed (Fig. 9; S3 sample bed; 13 to 27%). Bed bases are sharp, loaded and erosive, comprising abundant ENE–WSW oriented grooves and planar to undulatory sharp tops. Beds are structureless, with poorly-developed diffuse planar lamination (S10 sample bed) that usually occupies the upper half of beds, although it can be developed from base to top. Beds are coarse-grained to medium or fine-grained, weakly normally graded to ungraded and poorly sorted, comprising a wide grain-size range, especially at the lower half (S3 sample bed; from very fine to granule). Locally, faint planar laminations or hummock-like bedforms develop near bed tops (Fig. 9; S5 sample bed).

Interpretation: The high matrix content (up to 40%) and poor sorting suggest deposition from UTPF/QLPFs (Baas *et al.*, 2009, 2011, 2016) characterized by an abrupt loss in capacity (Hiscott, 1994a), high sediment fallout and reduced tractional reworking (Talling *et al.*, 2012). The crude normal grading and upward increasing matrix suggest some turbulence at the base of the parental flow, although the dominant rheology was likely an intermediate yield strength laminar flow (Talling *et al.*, 2012). However, the abundance of grooves can be linked to the development of a laminar plug at the base of these flows or a forerunning and bypassing debris flow (Baas *et al.*, 2021), which leads to entrainment of sediments (flow bulking, *sensu* Haughton *et al.*, 2009). Structured tops, if present, suggest mixing with ambient water at the rear or upper parts of the flow, which reduces viscosity and yield strength (Talling *et al.*, 2002; Sequeiros, 2012). Hummock-like bedforms are attributed to the development of combined flows with an oscillatory component, indicative of complex interaction between the parental flow and topography (Tinterri, 2011; Tinterri *et al.*, 2016) or supercritical flow development (Cartigny *et al.*, 2014, and references therein).

Type G beds

Description: Thick-bedded (0.5 to 6.0 m) sandy mudstone with sharp, erosive bases and undulatory tops. Type G beds contain abundant outsized, subangular sandstone clasts (0.05 to 1.0 m) supported by a poorly sorted and argillaceous matrix (Fig. 3). A medium-grained massive sandstone can locally underlie the argillaceous thick-bedded deposits with basal grooves containing deformed mudstone clasts (0.5 to 8.0 cm diameter; Privat *et al.*, 2021).

Interpretation: The outsized clasts supported within the argillaceous matrix suggest cohesive freezing from intermediate to high yield strength debris flows (Fig. 3; Talling *et al.*, 2012; Sohn, 1997). Erosive bed bases and the presence of sandstone clasts suggest that the source flows entrained compacted substrate (Dakin *et al.*, 2013; Hodgson *et al.*, 2019; Martínez-Doñate *et al.*, 2021). Alternatively, the debrites can also represent scour-fills post-dating previous erosive and bypassing flows. Mixing the cohesive laminar flow with ambient water might have diluted the basal part of the flow (Hampton, 1970; Mohrig *et al.*, 1998; Marr *et al.*, 2001). Therefore, both divisions are co-genetic (HEB type 1 of Privat *et al.*, 2021), with the basal sandstone representing deposition from a flow cohesive enough to develop grooves (Peakall *et al.*, 2020), such as lower to UTPF (Baas *et al.*, 2009). Due to their high matrix strength and to avoid confusion with other bed types (especially Type D, E and F beds), Type G beds are referred to as debrites, despite the local development of transitional flow behaviour near their base.

Type H beds

Description: Thin to thick (0.1 to 4.0 m) sandstones with sharp bases and tops, containing abundant grooves on both margins. These sandstones are massive, fine to medium-grained and well-cemented, although rare parallel striations are present on blistered surfaces (1 cm high and <2 cm diameter; see Cobain *et al.*, 2017) are also observed. They contain abundant mudstone clasts (2 to 5 cm diameter) and angular heterolithic rafts (10 to 50 cm length) that are oriented parallel to the bedding contacts (Fig. 3). Sub-horizontal thick sandstones cross-cut the stratigraphy at low angles (<15°). Thick sandstones develop branching of thin-bedded sub-vertical bodies (<0.2 m thick) of similar lithology that cross-cut the stratigraphy at various angles (15° to 90°).

Interpretation: These features are clastic injectites associated with compaction-driven fluid expulsion (Hurst *et al.*, 2011). The sub-horizontal thick sandstones are clastic sills with associated clastic dykes. Grooves at the base and top suggest laminar flow through lateral pressure transfer (Cobain *et al.*, 2015).

PETROGRAPHY

Petrological analysis of the 40 thin sections allowed us to determine the matrix content, grain size and mineral composition of Type A to F beds (Figs 4, 5, 6, 7, 8 and 9). Matrix represents a significant component in the analysed samples, ranging from 3.5 to 40.3% and 19.8% on average. Most sampled beds show an increase in matrix content from base to top, with a few exceptions where the matrix content decreases upward (S4 and S8 sample beds; Figs 5 and 8). The thick-bedded sandstones, where point contacts dominate, contain less matrix than the thin-beds, which are matrix-supported. Samples are characterized by a wide grain-size range, varying from silt to granular, with the mean and median grain size being fine to medium-sand. Overall, bed bases are generally coarser, and the mean grain size decreases upward within the same event bed. This pattern is well-developed in low-density and high-density turbidites (Type A and B; Figs 4 and 5) and banded TFDs (Type C; Fig. 6). In contrast, HEBs (Type D and E; Figs 7 and 8) and TFDs (Type F; Fig. 9) can show ungraded profiles. When traced laterally, the grain size also decreases across the vertical profile of the event beds, developing (very) fine-grained and matrix-rich pinch-outs. High-density turbidites (Fig. 5; Type B) and thick-bedded TFDs (Fig. 9; Type F) are the deposits that comprise the coarsest grain sizes (medium to coarse sand), whereas the rest is finer (very fine to medium sand; Fig. 10).

Compositional trends

Description: The analysed samples were plotted on standard monocrystalline quartz–feldspar–lithoclasts (Qm–F–Lt; Dickinson *et al.*, 1983), volcanic–metamorphic–sedimentary lithoclasts (Lv–Lm–Ls; Ingersoll & Suczek, 1979) and polycrystalline quartz–volcanic lithoclasts–sedimentary and metamorphic lithoclasts (Qp–Lv–Lsm; Dickinson, 1985) ternary diagrams (Fig. 11). In the Qm–F–Lt diagram (Dickinson *et al.*, 1983), nine samples plot in the recycled orogenic field, nine in the mixed field, and twenty-two in the magmatic arc field (Fig. 11A). From those twenty-two samples, nineteen correspond to the dissected arc field, whereas three are in the transitional arc field. The Lv–Lm–Ls diagram (Ingersoll & Suczek, 1979) reveals the dominance of volcanic lithoclasts over the other two lithic fragment types by plotting thirty-seven samples on the back-arc basin field and three on the fore-arc basin field (Fig. 11B). The Qp–Lv–Lsm diagram (Dickinson, 1985) plots twenty-seven samples on the magmatic arc field and thirteen on the mixed field (Fig. 11C).

Interpretation: The petrographic work and later plotting of the collected samples into different ternary diagrams reveal a consistent provenance field for the Early Jurassic Los Molles Formation in the Chachil Graben corresponding to the magmatic arc (Fig. 11; Burgess *et al.*, 2000) and supported by the north-east-directed palaeocurrents. Therefore, mixed source areas are unlikely to be responsible for the observed differences in depositional architecture and bed types within and between the Lower and Upper Lobe Complexes.

LOBE SUB-ENVIRONMENTS

The studied bed types are stacked into 3 to 7 m thick composite stratal units, bounded at the base and top by 0.2 to 1.0 m thick regional and walkable mudstones and/or debrites (Figs 12 and 13). These sandstone-rich packages represent intraslope lobes (Privat *et al.*, 2021). Three bed type associations are identified based on interpreted sedimentary processes and depositional environments. These bed type associations represent lobe sub-environments, including lobe axis, lobe off-axis and lobe fringe. The lobes of each lobe complex show a different transition from axial to fringe sub-environments, which impacted the architecture of the individual lobes and the lobe complexes. In the lobes of the Lower Lobe Complex, the lobe axis passes to the lobe off-axis in *ca* 1 km and into the lobe fringe over 0.5 km and pinching out in *ca* 1 km (Fig. 12), whereas within the Upper Lobe Complex, the lobe axis passes into the lobe off-axis over a horizontal distance of *ca* 1.2 km, and from off-axis to fringe environments over 0.8 km and pinching out in *ca* 1.3 km (Fig. 12).

Lobe axis

Description: This lobe sub-environment is characterized by amalgamated medium to thick-

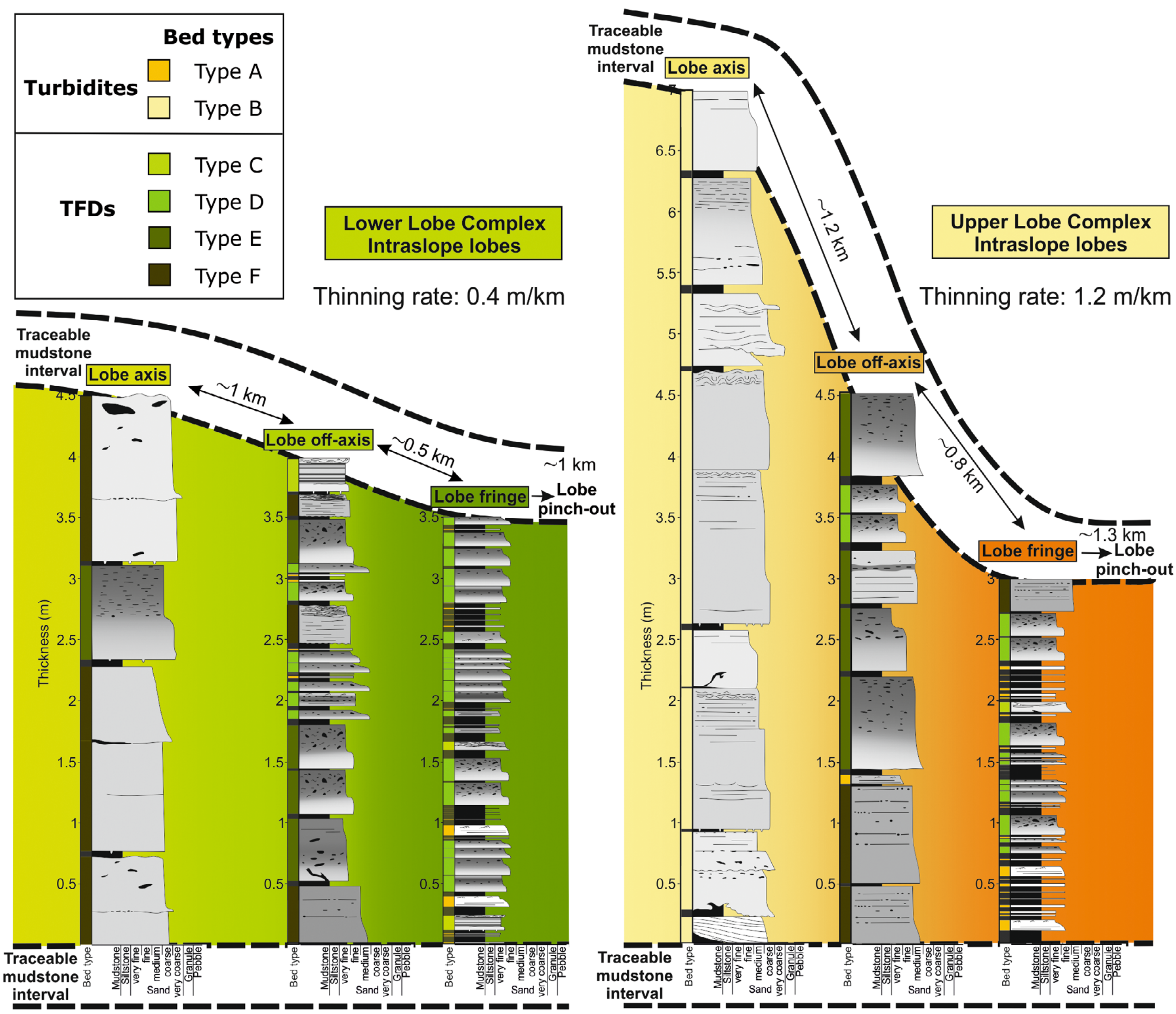

Fig. 12. Bed type association representing lobe sub-environments: axis, off-axis and fringe of Lower and Upper Lobe Complexes.

bedded sandstones (<1.2 m thick) forming stratal packages with rare mudstone intervals between the sandstone beds (<0.1 m thick; Fig. 12). The lobe axes within the Lower Lobe Complex are *ca* 4.5 m thick and dominated by TFDs, with Type F beds dominating over Type E beds (Fig. 12). In contrast, the lobe axes of the Upper Lobe Complex are *ca* 7 m thick and entirely dominated by thick-bedded, matrix-poor high-density turbidites (Type B beds; Fig. 12).

Interpretation: The highly amalgamated thick-bedded package represents a proximal environment dominated by deposition from energetic and high-concentration flows, supporting a lobe axis interpretation (Hodgson *et al.*, 2006; Prélat *et al.*, 2009; Spychala *et al.*, 2015). In the Lower Lobe Complex, the elevated concentration, cohesiveness and high-deceleration rates promoted the development of the transitional flow deposit (TFD)-dominated lobe axis comprising thick, amalgamated beds. In contrast, the axial parts of lobes in the Upper Lobe Complex were formed under erosional high-density turbidity currents. Despite the abundant mudstone clasts in Type B beds, no critical flow transformation developed due to the limited disaggregation of any contained clay, enabling preferential deposition of the coarsest grain fraction, and producing partial bypass of the finer sediments to more distal, down-current areas (Mutti & Ricci Lucchi, 1972; Mutti, 1992; Kneller & McCaffrey, 2003; Stevenson *et al.*, 2015).

Lobe off-axis

Description: Well-stratified, heterolithic successions of mudstones (<0.1 m thick) and medium-bedded sandstones characterize the lobe off-axis sub-environment. The lobe off-axis shows a lower sandstone–mudstone proportion than the lobe axis due to the lower bed thickness and a reduced level of bed amalgamation (Fig. 12). Sandstone beds in the Lower Lobe Complex are thinner (0.1 to 0.5 m thick) than in the Upper Lobe Complex (0.1 to 0.7 m thick). The lobe off-axis deposits of lobes in the Lower Lobe Complex are *ca* 4 m thick and dominated by thin to medium-bedded HEBs (Type D and E). However, subsidiary thick-bedded TFDs (Type F), banded TFDs (Type C) and low-density turbidites (Type A) are also observed. The lobe off-axis deposits of the lobes within the Upper Lobe Complex are *ca* 4.5 m thick and show less variability and thicker deposits. It is dominated by thick-bedded TFDs (Type F) and medium to thick-bedded HEBs (Type E), and rare low-density turbidites (Type A).

Interpretation: The range of thin to thick-bedded argillaceous deposits documented within the lobe off-axis suggests a sub-environment of deposition characterized by high-concentration flows with variable internal stratification and rheology. The dominance of TFDs with mudstone clasts indicates substrate entrainment and flow bulking (Haughton *et al.*, 2009), which increases flow cohesion and concentration. Entrainment and disaggregation of clay promote the formation of oversaturated and cohesive flows (Kane *et al.*, 2017) that could not transport their sediment load to distal parts of the lobe, thus promoting capacity-driven deposition (Hiscott, 1994a). Type C beds are interpreted as the product of a more moderate flow transformation and deceleration rate, where the cohesive forces are not dominant enough to produce flow collapse (Stevenson *et al.*, 2020). The differences between the lobe off-axis deposits of the Lower and Upper Lobe Complexes (amalgamation, thickness and variability of the deposits) lie in the behaviour of the source flows and their depositional character in the proximal sub-environment (lobe axis). In the Lower Lobe Complex, as the thick-bedded TFDs and HEBs were already deposited in the lobe axis, the flows reaching the lobe off-axis developed thinner deposits (Type C, D and E beds). In contrast, in the Upper Lobe Complex, the high-density turbidity currents transformed into transitional flows over longer distances, leading to high-density turbidite-dominated (Type B beds) lobe axis and medium to thick-bedded TFD-dominated (Type E and F beds) lobe off-axis.

Lobe fringe

Description: This lobe sub-environment is characterized by a well-stratified, fine-grained heterolithic succession composed of mudstones (<0.25 m thick) and thin sandstone beds (<0.3 m thick). The sandstone–mudstone proportion is lower than the lobe axis and off-axis sub-environments (Fig. 12). Overall, lobe fringes from the Lower and Upper Lobe Complex are similar, being *ca* 3 m thick (Fig. 12). Both comprise thin-bedded HEBs (Type D beds), banded TFDs (Type C beds) and low-density turbidites (Type A beds). However, the Lower Lobe Complex shows a higher proportion of thin-bedded HEBs (Type D beds), whereas the Upper Lobe

Complex comprises a higher proportion of low-density turbidites (Type A beds) and rare medium-bedded HEBs (Type E beds).

Interpretation: The thin-bedded heterolithic packages and lack of bed amalgamation suggest deposition in distal lobe settings. Thin-bedded HEBs (Type D beds) support flow transformation across the entire lobe, with flows that could not carry the sediment for a longer distance due to low flow cohesiveness, high deceleration rate, or both (Kane *et al.*, 2017). The other fundamental deposit, the low-density turbidites (Type A beds), are related to the source flow's high flow efficiency and dilute nature, which largely bypasses proximal lobe sub-environments and are deposited in distal areas. Such flows are deflected and reflected from intrabasinal relief without collapsing, reworking the sediment and developing bidirectional ripple lamination (e.g. Kneller & McCaffrey, 1999). In these relatively distal sub-environments, banded TFDs (Type C beds) developed through flow deceleration, enhancing the cohesive forces over the turbulence (Stevenson *et al.*, 2020). The rare presence of medium-bedded HEBs (Type E) in the Upper Lobe Complex is likely to represent flow transformation over a long distance from efficient high-density turbidity currents, enabling sediment transport and deposition in distal areas.

INTRASLOPE LOBE COMPLEX ARCHITECTURE AND BED TYPE DISTRIBUTION

The bed type associations described in the previous section are spatially and genetically related, representing different sub-environments within intraslope lobes. These intraslope lobes are stacked, forming two lobe complexes (Lower and Upper Lobe Complex), each bounded at the base and top by a >4 m thick regional mudstone or an erosionally-based debrite (Type G beds; Fig. 13; log 1 to log 7).

The sandstone–mudstone proportion was quantified for each bed type within each lobe for both lobe complexes in three different areas based on 764 sandstone beds (Fig. 14A). Logs 1 to 4, 5 to 6 and 7 to 8 represent the proximal, medial and distal locations, respectively (Fig. 1C). Logs 9 to 11 were not included in this analysis due to limited coverage of the investigated stratigraphic interval.

Lower Lobe Complex

The Lower Lobe Complex is *ca* 45 m thick and contains 10 stacked intraslope lobes. Due to outcrop limitations, the study of the stacking patterns within the Lower Lobe Complex is limited; however, the juxtaposition of lobe axis/off-axis and lobe fringe environments have been demonstrated to record compensational stacking of lobes (Prélat & Hodgson, 2013), albeit with a strong aggradational component (see 'jig-saw architecture'; Marini *et al.*, 2015; Fig. 13). Additionally, an overall basinward stepping stacking pattern of successive lobe pinch-outs is observed, recording the forestepping trend for the lobe complex (Fig. 13). Lobes achieve a maximum thickness of 4.5 m and comprise the thickest (<1 m thick) sandstone beds in their proximal parts (logs 1 to 4). These lobes are almost tabular, showing thinning rates of *ca* 0.4 m/km (Fig. 12). However, lobes pinch out abruptly north-eastward (between logs 7 and 9) over a horizontal distance of 2.4 to 2.7 km (Figs 1 and 2; Picún Leufú).

Apart from a complicated stacking pattern, the Lower Lobe Complex also records variability in sandstone content and bed type from proximal to distal (Fig. 14A). When traced down-dip over 2.4 km, amalgamation and sandstone–mudstone ratio decrease from proximal and medial areas (0.65) to distal areas (0.21; Fig. 14A). In proximal (logs 1 to 4) and medial (logs 5 and 6) parts, TFDs (Type D, E and F) dominate over low-density turbidites (Type A bed; proximal: 84% and medial: 87%). In the distal parts (logs 7 and 8), beyond the pinch-out of most HEBs and thick-bedded TFD (Type D, E and F), low-density turbidites (Type A bed) dominate over TFDs (75%), with occasional thin-bedded banded sandstone (Type C bed; Fig. 14A).

Upper Lobe Complex

The Upper Lobe Complex is *ca* 30 m thick and contains five aggradationally stacked intraslope lobes (Fig. 13). The lobes are up to 7 m thick in proximal areas (logs 1 to 4), showing their highest amalgamation ratio and the thickest beds (up to 1.2 m thick; Fig. 12). The lobes thin north-eastward from *ca* 7 m to *ca* 3 m thick, showing thinning rates of 1.2 m/km (Fig. 12) and pinch out over a horizontal distance of *ca* 3.3 km (Fig. 11) between logs 10 and 11 (compaction hinge of El Luchador fault block; Figs 1 and 2).

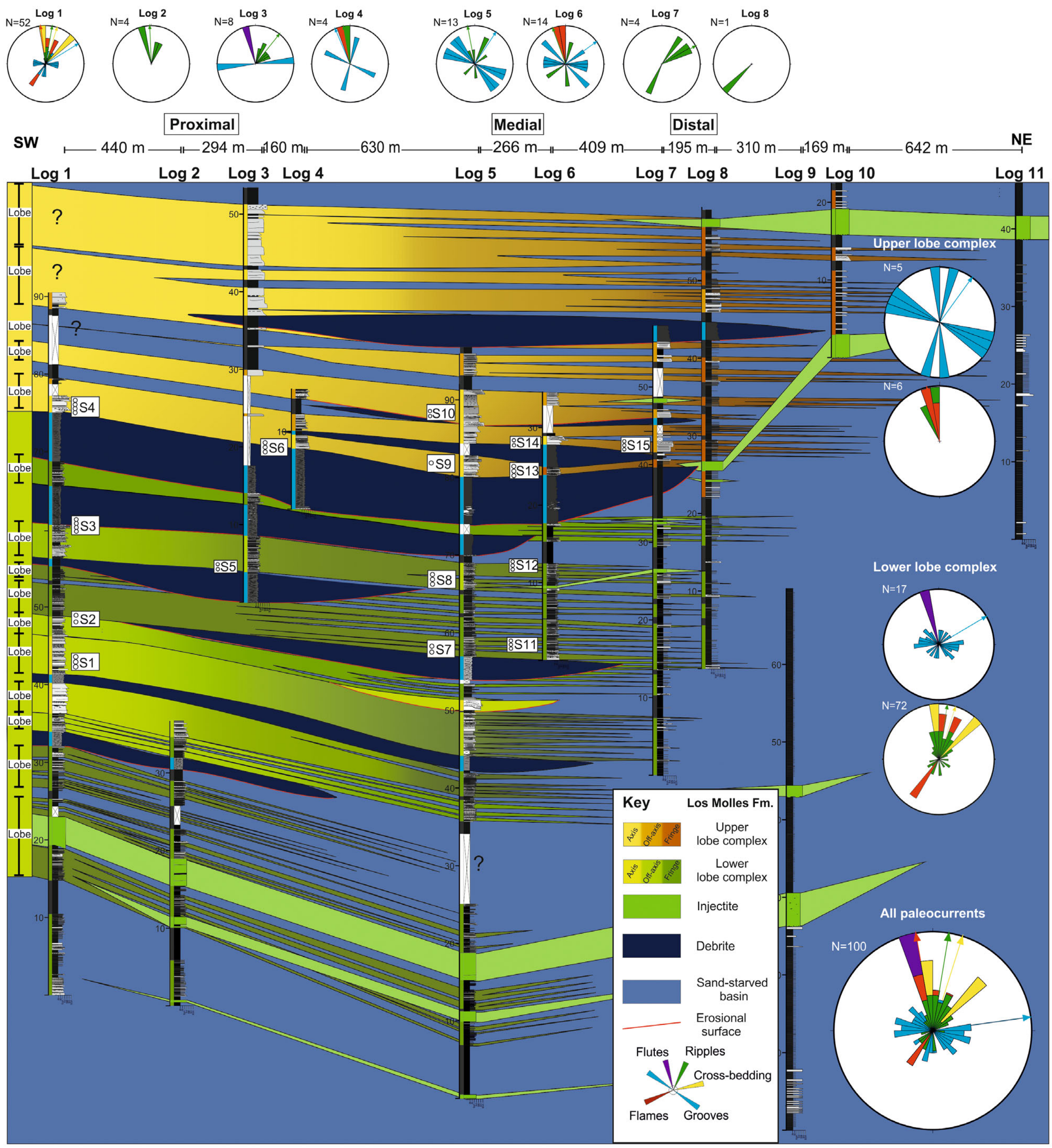

Fig. 13. Detailed correlation panel showing the different lobe sub-environments and the overall architecture and pinch-out positions of the two lobe complexes. Rose diagrams show palaeocurrents for each lobe complex and log. Tool marks show higher divergence than ripple lamination because denser flows/divisions are more sensitive to intrabasinal topography than dilute flows/divisions.

In proximal parts, the Upper Lobe Complex contains a sandstone–mudstone ratio of 0.66 and is dominated by high-density turbidites (Type B beds; 98%; Fig. 14A). In medial areas, the sandstone–mudstone proportion is 0.75, and TFDs (Type E and F) dominate over turbidites (Type B; 87.7%; Fig. 14A). In distal parts, there is an abrupt decrease in sandstone–mudstone

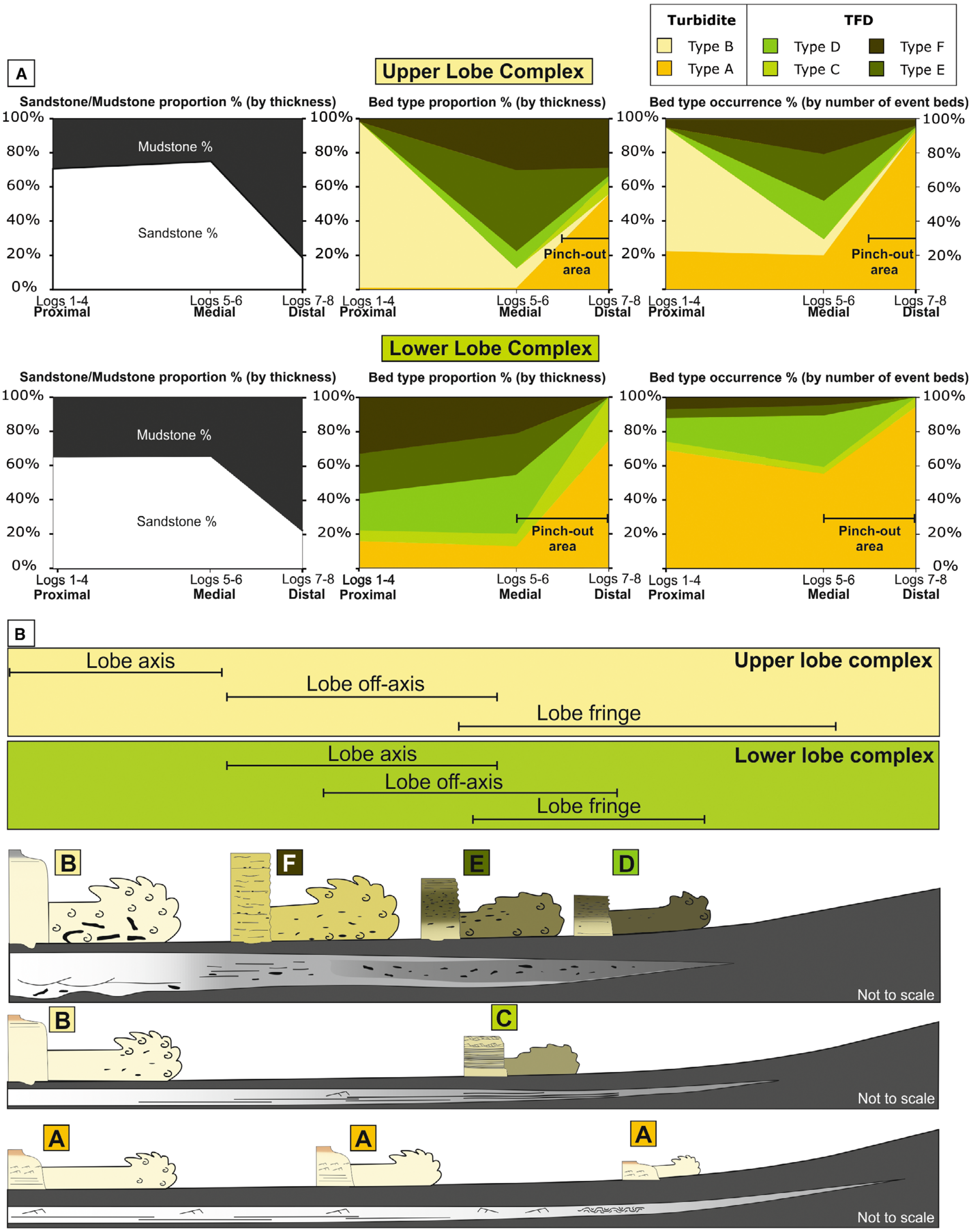

Fig. 14. (A) Graphs showing sandstone–mudstone proportion (left), bed type proportion (centre) and bed type occurrence (right) from both Lower and Upper Lobe Complexes in proximal (Log 1 to 4), medial (Log 5 to 6) and distal (Logs 7 to 8) parts of the Chachil Graben (see Fig. 1C for location). (B) Summary diagram of different flow evolution showing deposit variability from proximal to pinch-out areas. Denser flows tend to decelerate more abruptly and produce strong deposit variability, unlike dilute flows, which can maintain their efficiency (Mutti, 1979) for longer distances. The greater the incorporation of cohesive mud, the shorter the distance over which flows transform into low-efficiency cohesive flows, resulting in rapid flow collapse.

proportion (0.18), and low-density turbidites dominate (Type A beds) over TFDs and HEBs (55.8%; Fig. 14A).

DISCUSSION

Controls on bed types and flow transformation

The flow transformations responsible for the reported variability in bed types are proposed to have been controlled by the incorporation of clay from the substrate and the flow deceleration rates (Fig. 14B). It is suggested that the flow transformations observed here were characterized by the interplay between complex longitudinal and vertical flow segregation processes. Longitudinal flow processes are characterized by high concentration bypassing flow heads (e.g. Sohn *et al.*, 2002) responsible for the bedload transfer of mudstone clasts to slower and more depositional parts of the flow (Baas *et al.*, 2021). 'Self-accelerating' flow cells at the front of the flow have been reported in physical modelling (*sensu* Sequeiros *et al.*, 2009, 2018) and are increasingly recognized in modern systems (Azpiroz-Zabala *et al.*, 2017; Paull *et al.*, 2018; Pope *et al.*, 2022). However, in the rock record, evidence for the erosional and bypassing flow head is the abundance of grooves and high matrix content in Type B, C, D, E, F and G beds, as reported in this study. The formation of H1 divisions in Type C, D and E beds is inferred to be a product of transitional flows (Baker & Baas, 2020; Hussain *et al.*, 2020) rather than turbidites (Haughton *et al.*, 2003, 2009; Davis *et al.*, 2009). The inherited early post-rift topography (Fig. 15A; Privat, 2019; Privat *et al.*, 2021) likely promoted higher rates of flow deceleration, which could have led to the development of TFDs in proximal lobe sub-environments (Fig. 14B; e.g. Fonnesu *et al.*, 2015, 2018; Terlaky & Arnott, 2016; Brooks *et al.*, 2018a,b, 2022; Mueller *et al.*, 2021). In contrast, the non-erosional low-density turbidites remained almost tabular without any transition into other bed types (Fig. 14B), indicating more stable flow conditions and efficiency than the denser transitional flows (Mutti, 1979).

Sediment routing pathways and mud availability

The mudstone-dominated substrate could have enhanced the development of matrix-rich deposits (Fig. 14B). The >100 m thick mud-rich package that draped the syn-rift topography (Figs 2, 13 and 15A) was available for entrainment into the overriding flows. The availability and incorporation of the muddy substrate (Fonnesu *et al.*, 2015, 2018; Mueller *et al.*, 2021; Brooks *et al.*, 2022) could have been enhanced by the immature sediment routing pathways (Privat *et al.*, 2021), leading to poor channelization. Additionally, if the substrate was poorly-consolidated, it could have been easily entrained (Terlaky & Arnott, 2014; Kane *et al.*, 2017; Martínez-Doñate *et al.*, 2021), promoting flow bulking (Haughton *et al.*, 2009). Furthermore, poorly-developed sediment routing pathways are unlikely to be as effective as channel-levée systems in removing the fines through flow stripping and overspill (Peakall *et al.*, 2000; Hodgson *et al.*, 2016). These effects could explain the dominance of TFDs in the lobe axis of the Lower Lobe Complex (Figs 12 and 15B). This contrasts with previous studies documenting the sandy nature of instraslope lobes (e.g. Spychala *et al.*, 2015; Brooks *et al.*, 2018a,b). These models highlight the deposition of the coarser fraction in the more up-dip locations, while the more dilute fine-grained tops of the turbidity currents bypass down-dip (flow decoupling; Kneller & McCaffrey, 1999). However, in transitional flow-dominated systems, the cohesive lower part would deposit matrix-rich poorly sorted deposits (TFD) while the upper and dilute division bypasses. This effect could also explain the TFD-dominated nature of lobes within the Lower Lobe Complex.

Fig. 15. Schematic diagrams show (A) the response of parental sediment gravity flows (B) and the submarine lobe from the Lower and Upper Lobe Complexes in response to seafloor relief. The Lower Lobe Complex pinch-out is more proximal than the Upper Lobe Complex due to the flattening of the inherited early post-rift topography over time. Denser flows or parts of flows are restricted to the topographic lows, while the more dilute ones can travel further into the compaction hinge, depositing low-density turbidites. Note the positions of the logs marked by black squares.

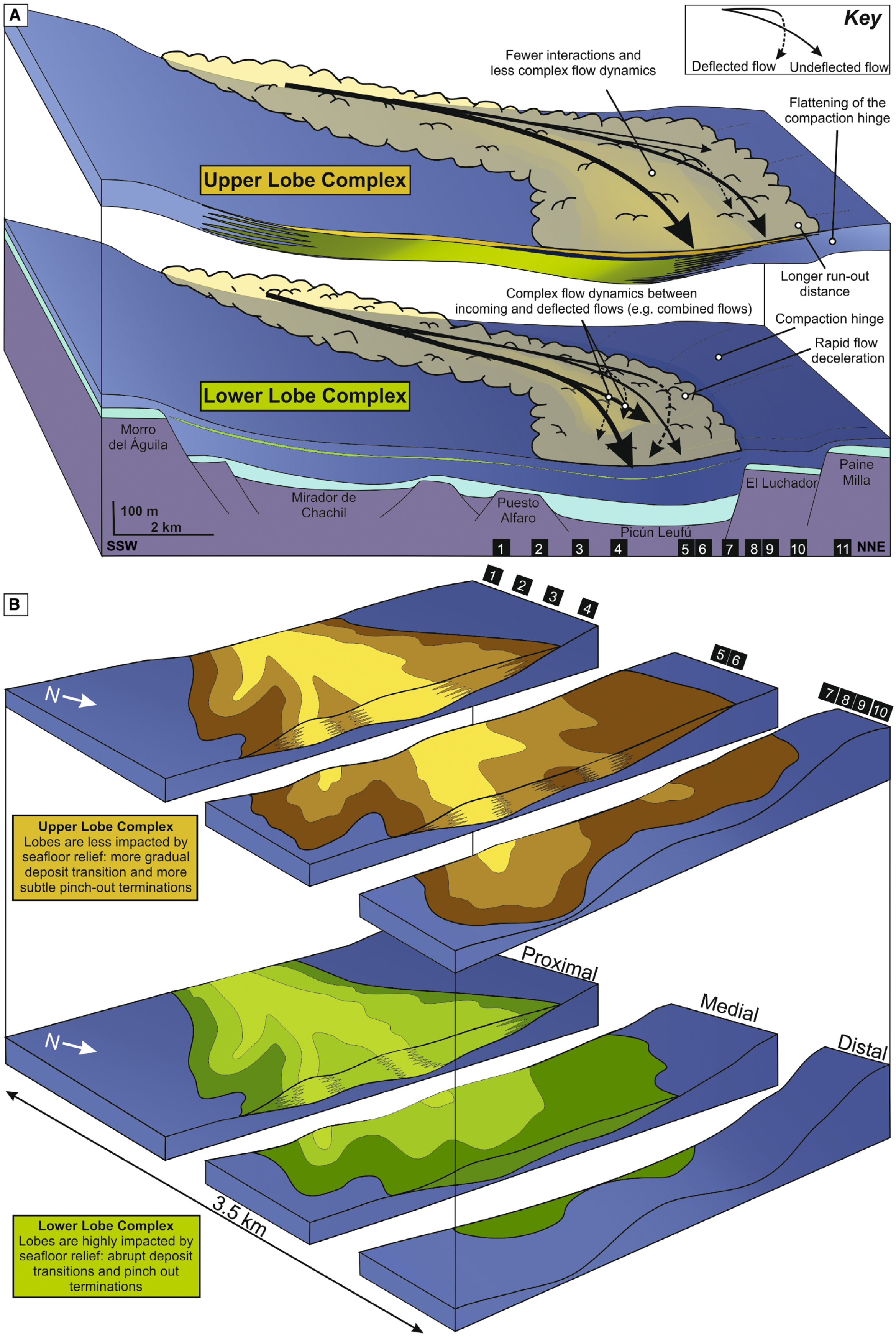
A
Key
Deflected flow
Undeflected flow
Fewer interactions and
less complex flow dynamics
Flattening of the
compaction hinge
Upper Lobe Complex
Longer run-out
distance
Complex flow dynamics between
incoming and deflected flows (e.g. combined flows)
Compaction hinge
Rapid flow
deceleration
Lower Lobe Complex
Morro
del Águila
Mirador de
Chachil
Puesto
Alfaro
Picún Leufú
El Luchador
Paine
Milla
100 m
2 km
SSW
NNE
1 2 3 4 5 6 7 8 9 10 11
B
1 2 3 4
5 6
7 8 9 10
N
Upper Lobe Complex
Lobes are less impacted by
seafloor relief: more gradual
deposit transition and more
subtle pinch-out terminations
Proximal
Medial
Distal
N
3.5 km
Lower Lobe Complex
Lobes are highly impacted by
seafloor relief: abrupt deposit
transitions and pinch out
terminations

In contrast, in the Upper Lobe Complex, flows travelled over sandier deposits (Fig. 13), which might have limited entrainment of the muddy substrate (Terlaky & Arnott, 2014). This interpretation is supported by the dominance of high-density turbidites in the lobe axis and TFDs and HEBs in lobe fringes (Fig. 15B). Bed type proportions in medial parts of the Upper Lobe Complex are comparable to the proportions in proximal parts of the Lower Lobe Complex (Fig. 14A). A similar effect is observed at the lobe scale, with lobe axes of the Lower Complex and lobe off-axis deposits of the Upper Lobe Complex comprising similar bed type associations despite the different degrees of bed amalgamation (Fig. 12). This study highlights the role that variable substrate entrainment can play in intraslope lobes with a similar source.

Impact of topography on the pinch-out pattern

Seafloor relief affects the deceleration rates of sediment gravity flows, impacting the character of deep-water deposits (Pantin & Leeder, 1987; Edwards, 1991; Kneller *et al.*, 1991; Edwards *et al.*, 1994; Kneller, 1995; Al-Ja'Aidi *et al.*, 2004). Depending on their flow properties, sediment gravity flows will respond differently when interacting with such relief, and this will influence the distribution of bed types in the lobes (Figs 12, 14B and 15B). The abruptness of pinch-out terminations (Al-Ja'Aidi *et al.*, 2004; Bakke *et al.*, 2013; Soutter *et al.*, 2019) is strongly controlled by the yield strength of the source flow with limited flow efficiency (Mutti, 1979; Hiscott, 1994a). This effect is observed in the Chachil Graben, where the lobe complex terminations offset the pinch-out of the contemporaneous debrites (Fig. 13). This effect is not limited to laminar flows; it also impacts the transitional flows producing thin-bedded, matrix-rich HEBs (Type D) that pinch out abruptly against the frontal topography (Fig. 14B). Denser flows are more sensitive to intrabasinal topography than dilute flows/divisions (e.g. Tőkés & Patacci, 2018). This statement is supported by the high divergence in palaeoflow reported from the multidirectional grooves, indicative of the sensitivity of TFDs (Peakall *et al.*, 2020) to obstacles (for example, debrite rugosity; Muzzi Magalhaes & Tinterri, 2010) and basin-scale topography (for example, compaction hinge; Fig. 15A). In contrast, the dilute (parts of) flows did not decelerate rapidly enough, or failed to entrain enough substrate mud, to suppress flow turbulence (Al-Ja'Aidi *et al.*, 2004; Talling *et al.*, 2012). This results in extensive thin-bedded low-density turbidites (e.g. Smith, 2004) or banded TFDs offsetting the pinch-out of HEBs, depositing on relative topographic highs, as seen with the pinch-out pattern documented in the study area (Fig. 14B). The ripple and flame structures indicate that proximal areas (logs 1 to 4) show an overall north-east trend, with deflection/reflection indicators (Fig. 13; Privat *et al.*, 2021). Another indicator of complex flow behaviour resulting from the interaction between transitional flows and seafloor relief is the development of hummock-type structures (Fig. 9; S5 sample bed). These structures are evidence of combined flows characterized by an oscillatory component produced by internal waves and reflected bores (Tinterri *et al.*, 2016). Combined-flow bedforms (S5 sample bed, Type F beds; Fig. 9) are well-developed in the Lower Lobe Complex, where a higher interaction with topography is inferred (Fig. 15A).

Steepness of the confining slope and comparison with other systems

Intraslope lobe complexes of the earliest Los Molles Formation were deposited under the influence of a south-facing, oblique counterslope formed by a compaction hinge above the El Luchador fault block (Privat *et al.*, 2021; Figs 2, 13 and 15). Reconstructing the steepness of the confining slope during this earliest post-rift stage is not straightforward, where onlap terminations against basin margins are not developed. Deep-water systems interacting with gentle topography (i.e. a fraction of a degree) tend to produce a complex pinch-out of the sand-rich lobe component, characterized by an aggradational succession of tens of metres of thin beds containing climbing ripples. Published examples include the Welsh Basin (Wales, UK) (Smith, 2004) and Karoo Basin (South Africa) (Spychala *et al.*, 2017a,b). In contrast, on steeper slopes (i.e. >10°), the characteristic termination style is onlap of sheet-like sandstone beds unconformably terminating directly onto the basin margin, such as in the Annot Basin, France (Kneller & McCaffrey, 1999; Sinclair, 2000; McCaffrey & Kneller, 2001; Bakke *et al.*, 2013; Soutter *et al.*, 2019) and the Laga Basin in Italy (Marini *et al.*, 2015). In the Chachil Graben, the abruptness of pinch-outs, lack of climbing ripple lamination, and the bed types reported in this contribution suggest that the compaction hinge-related counterslope was steeper (>1°) than those reconstructed for the Welsh (Smith, 2004) and Karoo Basin (Spychala *et al.*, 2017a,b) but less steep than those reported in the Annot (Du Fornel *et al.*, 2004; Soutter *et al.*, 2019) or Laga Basin (Marini *et al.*, 2015). Further quantifying the angle in the Chachil Graben is challenging due to the similarity between the organic-rich calcareous mudstones that draped the rift topography (Privat *et al.*, 2021) and the high-efficiency silty (Mutti, 1979), low-density turbidites offsetting the sandstones (distal fringe; Boulesteix *et al.*, 2020). In addition, post-depositional compaction-driven deformation (burial-related) and the draping nature of the more distal deposits might lead to overestimating the counterslope angle (Pickering & Hilton, 1998; Bakke *et al.*, 2013). Another indicator of seafloor relief is the presence of an injectite network (Figs 13 and 15A; Cobain *et al.*, 2017; Hansen *et al.*, 2019). This suggests that early post-rift topography is not solely limited to inheritance from the previous extensional phase but can be locally enhanced by compaction-related deformation, promoting long-lived seabed relief that largely influenced the nature of the intraslope lobes.

Controls on stratigraphic architecture

The differential flow deceleration and deposition produced by the frontal topography in the Chachil Graben promoted a thicker accumulation of lobe-related deposits over the depocentre lows than on the topographic highs (Figs 13, 15A and 15B; Smith & Joseph, 2004). In the Lower Lobe Complex, the abruptness of the pinch-out terminations, the tabularity of the intraslope lobes (4.5 m thick and <1 m thinning), and the multidirectional grooves and ripples suggest that a complex frontal seafloor topography was a strong control on geometry and architecture. The Lower Lobe Complex (*ca* 45 m thick) is characterized by a progressive down-dip advancement of the pinch-out position from base to top (Figs 13 and 15A). This pinch-out pattern suggests infilling, flattening and smoothing the complex inherited rift topography over time (Fig. 15B; e.g. Ross *et al.*, 1994; Hay, 2012). The stacking of 10 intraslope lobes shows a compensational pattern (e.g. Mutti & Sonnino, 1981; Deptuck *et al.*, 2008; Prélat *et al.*, 2009) with a strong aggradational component, where topography confined the lobes frontally but enabled lateral compensation. The authors interpret that during the deposition of the Lower Lobe Complex, the deep-water system was confined (Winker, 1996; Sinclair, 2000; Southern *et al.*, 2015) at the lobe scale but semi-confined (Marini *et al.*, 2015; Dodd *et al.*, 2019) at the lobe complex scale. In the Upper Lobe Complex (*ca* 30 m thick), the five intraslope lobes are thicker (7 m thick), show lower thinning rates and can be traced over longer distances (>3.3 km) than in the Lower Lobe Complex. This architecture and termination style suggest that seafloor topography impacted individual lobes less. Given that the pinch-out terminations developed over the compaction hinge, flows were likely to deflect towards the east (north-east) after interacting with the south/south-west-dipping oblique-to-frontal oriented (see Kneller *et al.*, 1991; Soutter *et al.*, 2021) compaction hinge. The five intraslope lobes show an aggradational stacking pattern, juxtaposing similar sub-environments on top of one another. This reveals that, even if the Upper Lobe Complex and its lobes recorded a reduction in frontal confinement (compared to the Lower Lobe Complex), the system was more confined laterally at the lobe complex scale, limiting lobe-scale compensational stacking. In other words, the stratigraphic evolution presented here shows an upward decrease in frontal confinement at both lobe and lobe complex scales; however, there is an increase in the degree of lateral confinement. The authors postulate that the increasingly aggradational stacking pattern recorded from the Lower to the Upper Lobe Complex is unrelated to depocentre-scale topographic modification but rather to an increase in sediment input and flow efficiency (Mutti, 1979). Additionally, the continuous slope degradation and emplacement of debrites might have flattened the topography, favouring the connectivity along the slope and efficiency of the flows. This highlights that the concept of confinement is related to the balance between the accommodation and the size of the depositional system and their source flows. Considering the two lobe complexes as a lobe complex set (Prélat *et al.*, 2009), this larger unit shows a progradational stacking pattern (e.g. Hodgson *et al.*, 2006; Grundvåg *et al.*, 2014) related to the maturation of the sediment routing pathway (Hodgson *et al.*, 2016) and smoothing of the inherited topography (Fig. 15A and B). This study highlights the impact of inherited early post-rift topography in deep-water siliciclastic systems, from the bed-scale to lobe complex-scale (Jackson *et al.*, 2008; Privat *et al.*, 2021).

Los Molles intraslope lobes as an analogue for subsurface lobe systems

This section discusses the Los Molles intraslope lobes as an analogue for subsurface reservoirs for hydrocarbon extraction or carbon storage. Grain size, sorting, matrix content and distribution are key parameters controlling porosity and permeability values (e.g. Bell *et al.*, 2018). Overall, the mean grain size, amalgamation and sandstone/mudstone proportions decrease from lobe axes to fringes, whereas matrix content and sorting increase. The deposits found at the lobe axis are likely to comprise the best reservoir properties of the lobes due to the abundance of high-density turbidites (only in the Upper Lobe Complex) and the high degree of amalgamation, which promotes communication between sandstone beds (Begg & King, 1985; Desbarats, 1987; Deutsch, 1989). In contrast, the decrease in amalgamation, grain size and the development of argillaceous deposits or divisions in the lobe-off axis and lobe fringe environments may result in decreasing permeability values (intrabed baffles; Porten *et al.*, 2016; Southern *et al.*, 2017; Bell, 2019).

The development of abrupt HEB-rich frontal pinch-outs, and confinement produced by compaction-related topography, suggests a high stratigraphic trapping potential with reduced leakage risk. The coarser grain sizes and less argillaceous deposits of the Upper Lobe Complex suggest higher permeability values than the TFD-dominated Lower Lobe Complex (e.g. Southern *et al.*, 2017). However, in the subsurface, the matrix content does not necessarily hinder the reservoir properties because the volume of clay coating around grains, such as chlorite, can inhibit quartz cement growth and, therefore, preserve primary porosity (Heald & Larese, 1974; Ehrenberg, 1993; Anjos *et al.*, 1999; Dowey *et al.*, 2012). In addition, the development of injectites that pinch out within the mudstones suggests that sand bodies are sealed and may form stratigraphic traps (post-depositional; Hurst *et al.*, 2005, 2008; Scott *et al.*, 2013) although, in some cases, they can also represent leakage paths (Monnier *et al.*, 2014; Cobain *et al.*, 2017). Further studies that integrate detailed petrographic and architectural data in these and similar deposits are needed to improve our understanding of how these systems might act as hydrocarbon reservoirs, aquifers and carbon or hydrogen storage sites.

CONCLUSIONS

Field mapping, log correlation and facies analysis of two exhumed early post-rift intraslope lobe complexes show consistently different characteristics. Characterization at grain-scale using quantitative petrographic methods suggests that transitional flow deposits dominate the argillaceous Lower Lobe Complex, and beds pinch out more abruptly than in the overlying turbidite-dominated Upper Lobe Complex. Compositional analysis suggests that both lobe complexes are volcanic arc sourced and, therefore, that the source area was not responsible for the differences in bed types between the lobe complexes. The preferred interpretation is an autogenic response of the depositional system due to the progressive healing of intraslope relief, maturation of sediment transport routes, and reduction in mud entrainment from the substrate. The compaction hinge(s) acted as a barrier for the denser and cohesive (parts of) flows, but the dilute turbidity currents could override and deposit on the intrabasinal slope. This study highlights the primary role of subtle inherited relief developed during the early post-rift stage of basin development. This integrated petrographic, architectural and sedimentary process model provides new insights into how these systems act as hydrocarbon reservoirs, aquifers and carbon storage sites. A better understanding of grain type and grain-size segregation from proximal to distal parts of deep-water systems is critical for carbon sequestration and predicting CO_2 plume dynamics.

ACKNOWLEDGEMENTS

This study is a collaboration between The University of Manchester (UK), The University of Leeds (UK), Imperial College (UK) and Centro de Investigaciones Geológicas (CIG; Argentina). The authors thank Eduardo Zinni and other local farmers for permitting field studies on their land. The LOBE 3 consortium project of which this research forms a part is supported by sponsorship from Aker BP, BHP, BP, Equinor, HESS, Neptune, Petrobras, PetroChina, Total, *Vår Energi and W*oodside, for which the authors are grateful. We would like to thank reviewers Benjamin Kneller and an anonymous reviewer for their thoughtful reviews, and Associate Editor Victoria Valdez and Chief Editor Jaco Baas for additional helpful comments that improved the manuscript.

CONFLICT OF INTEREST

The authors declare no conflict of interest for this work.

DATA AVAILABILITY STATEMENT

The data that support the findings of this study are available from the corresponding author.

REFERENCES

Al-Ja'Aidi, O.S., **McCaffrey, W.D.** and **Kneller, B.C.** (2004) Factors influencing the deposit geometry of experimental turbidity currents: implications for sand-body architecture in confined basins. *Geol. Soc. London Spec. Publ.*, **222**, 45–58.

Amy, L.A., **Talling, P.J.**, **Edmonds, V.O.**, **Sumner, E.J.** and **Lesueur, A.** (2006) An experimental investigation of sand-mud suspension settling behaviour: implications for bimodal mud contents of submarine flow deposits. *Sedimentology*, **53**, 1411–1434.

Anjos, S.M.C., **De Ros, L.F.** and **Silva, C.M.A.** (1999) Chlorite Authigenesis and porosity preservation in the upper cretaceous marine sandstones of the Santos Basin, offshore eastern Brazil. *Clay Miner. Cem. Sandstones*, 289–316.

Argent, J.D., **Stewart, S.A.** and **Underhill, J.R.** (2000) Controls on the lower cretaceous punt sandstone member, a massive deep-water clastic deposystem, inner Moray firth, UK North sea. *Pet. Geosci.*, **6**, 275–285.

Arnott, R.W.C. and **Al-Mufti, O.** (2017) Deep-marine pseudo dune cross-stratification-similar, but completely different. *J. Sed. Res.*, **87**, 312–323.

Azpiroz-Zabala, M., **Cartigny, M.J.B.**, **Talling, P.J.**, **Parsons, D.R.**, **Sumner, E.J.**, **Clare, M.A.**, **Simmons, S.M.**, **Cooper, C.** and **Pope, E.L.** (2017) Newly recognized turbidity current structure can explain prolonged flushing of submarine canyons. *Sci. Adv.*, **3**, e1700200.

Baas, J.H., **Best, J.L.**, **Peakall, J.** and **Wang, M.** (2009) A phase diagram for turbulent, transitional, and laminar clay suspension flows. *J. Sed. Res.*, **79**, 162–183.

Baas, J.H., **Best, J.L.** and **Peakall, J.** (2011) Depositional processes, bedform development and hybrid bed formation in rapidly decelerated cohesive (mud-sand) sediment flows. *Sedimentology*, **58**, 1953–1987.

Baas, J.H., **Best, J.** and **Peakall, J.** (2016) Predicting bedforms and primary current stratification in cohesive mixtures of mud and sand. *J. Geol. Soc. London*, **173**, 12–45.

Baas, J.H., **Tracey, N.D.** and **Peakall, J.** (2021) Sole marks reveal deep-marine depositional process and environment: implications for flow transformation and hybrid-event-bed models. *J. Sed. Res.*, **91**, 986–1009.

Baker, M.L. and **Baas, J.H.** (2020) Mixed sand–mud bedforms produced by transient turbulent flows in the fringe of submarine fans: indicators of flow transformation. *Sedimentology*, **67**, 2645–2671.

Bakke, K., **Kane, I.A.**, **Martinsen, O.J.**, **Petersen, S.A.**, **Johansen, T.A.**, **Hustoft, S.**, **Jacobsen, F.H.** and **Groth, A.** (2013) Seismic modeling in the analysis of deep-water sandstone termination styles. *Am. Assoc. Pet. Geol. Bull.*, **97**, 1395–1419.

Barker, S.P., **Haughton, P.D.W.**, **McCaffrey, W.D.**, **Archer, S.G.** and **Hakes, B.** (2008) Development of rheological heterogeneity in clay-rich high-density turbidity currents: Aptian Britannia sandstone member, U.K. Continental shelf. *J. Sed. Res.*, **78**, 45–68.

Begg, S.H. and **King, P.R.** (1985) Modelling the effects of shales on reservoir performance: calculation of effective vertical permeability. In: *SPE Reservoir Simulation Symposium*. OnePetro. https://doi.org/10.2118/13529-MS

Bell, D. (2019) Prediction of reservoir properties from processes and architecture in deep-water clastic systems. A Thesis submitted to the University of Manchester for the degree of doctor of philosophy in the Faculty of Science and Engineering.

Bell, D., **Kane, I.A.**, **Pontén, A.S.M.**, **Flint, S.S.**, **Hodgson, D.M.** and **Barrett, B.J.** (2018) Spatial variability in depositional reservoir quality of deep-water channel-fill and lobe deposits. *Mar. Pet. Geol.*, **98**, 97–115.

Best, J. and **Bridge, J.** (1992) The morphology and dynamics of low amplitude bedwaves upon upper stage plane beds and the preservation of planar laminae. *Sedimentology*, **39**, 737–752.

Boulesteix, K., **Poyatos-Moré, M.**, **Hodgson, D.M.**, **Flint, S.S.** and **Taylor, K.G.** (2020) Fringe or background: characterizing deep-water mudstones beyond the basinfloor fan sandstone pinchout. *J. Sed. Res.*, **90**, 1678–1705.

Brooks, H.L., **Hodgson, D.M.**, **Brunt, R.L.**, **Peakall, J.**, **Hofstra, M.** and **Flint, S.S.** (2018a) Deep-water channel-lobe transition zone dynamics: processes and depositional architecture, an example from the Karoo Basin, South Africa. *Bull. Geol. Soc. Am.*, **130**, 1723–1746.

Brooks, H.L., **Hodgson, D.M.**, **Brunt, R.L.**, **Peakall, J.**, **Poyatos-Moré, M.** and **Flint, S.S.** (2018b) Disconnected submarine lobes as a record of stepped slope evolution over multiple sea-level cycles. *Geosphere*, **14**, 1753–1779.

Brooks, H.L., **Ito, M.**, **Zuchuat, V.**, **Peakall, J.** and **Hodgson, D.M.** (2022) Channel-lobe transition zone development in tectonically active settings: implications for hybrid bed development. *Depos. Rec.*, **8**, 1–40.

Burgess, P.M., **Flint, S.** and **Johnson, S.** (2000) Sequence stratigraphic interpretation of turbiditic strata: an example from Jurassic strata of the Neuquén basin, Argentina. *Bull. Geol. Soc. Am.*, **112**, 1650–1666.

Burgreen, B. and **Graham, S.** (2014) Evolution of a deep-water lobe system in the Neogene trench-slope setting of the East Coast Basin, New Zealand: lobe stratigraphy and architecture in a weakly confined basin configuration. *Mar. Pet. Geol.*, **54**, 1–22.

Cartigny, M.J.B., **Ventra, D.**, **Postma, G.** and **van Den Berg, J.H.** (2014) Morphodynamics and sedimentary structures of bedforms under supercritical-flow conditions: new insights from flume experiments. *Sedimentology*, **61**, 712–748.

Ciccioli, P.L., **Limarino, C.O.**, **Friedman, R.** and **Marenssi, S.A.** (2014) New high precision U-Pb ages for the Vinchina formation: implications for the stratigraphy of the Bermejo Andean foreland basin (La Rioja province, western Argentina). *J. S. Am. Earth Sci.*, **56**, 200–213.

Cobain, S.L., **Peakall, J.** and **Hodgson, D.M.** (2015) Indicators of propagation direction and relative depth in clastic injectites: implications for laminar versus turbulent flow processes. *Bull. Geol. Soc. Am.*, **127**, 1816–1830.

Cobain, S.L., **Hodgson, D.M.**, **Peakall, J.** and **Shiers, M.N.** (2017) An integrated model of clastic injectites and basin floor lobe complexes: implications for stratigraphic trap plays. *Basin Res.*, **29**, 816–835.

Cristallini, E., **Tomezzoli, R.**, **Pando, G.**, **Gazzera, C.**, **Martínez, J.M.**, **Quiroga, J.**, **Marianso, B.**, **Bechis, F.**, **Barredo, S.** and **Zambrano, O.** (2009) Controls of the Precuyano in the structure of the Neuquén Basin. *Rev. Asoc. Geol. Argentina*, **65**, 248–264.

Cullen, T.M., **Collier, R.E.L.**, **Gawthorpe, R.L.**, **Hodgson, D.M.** and **Barrett, B.J.** (2020) Axial and transverse deep-water sediment supply to syn-rift fault terraces: insights from the West Xylokastro fault block, gulf of Corinth, Greece. *Basin Res.*, **32**, 1115–1149.

Curray, J.R., **Emmel, F.J.** and **Moore, D.G.** (2002) The Bengal fan: morphology, geometry, stratigraphy, history and processes. *Mar. Pet. Geol.*, **19**, 1191–1223.

Dakin, N., **Pickering, K.T.**, **Mohrig, D.** and **Bayliss, N.J.** (2013) Channel-like features created by erosive submarine debris flows: field evidence from the middle Eocene Ainsa Basin, Spanish Pyrenees. *Mar. Pet. Geol.*, **41**, 62–71.

Davis, C., **Haughton, P.**, **McCaffrey, W.**, **Scott, E.**, **Hogg, N.** and **Kitching, D.** (2009) Character and distribution of hybrid sediment gravity flow deposits from the outer forties fan, Palaeocene Central North Sea, UKCS. *Mar. Pet. Geol.*, **26**, 1919–1939.

Deptuck, M.E., **Piper, D.J.W.**, **Savoye, B.** and **Gervais, A.** (2008) Dimensions and architecture of late Pleistocene submarine lobes off the northern margin of East Corsica. *Sedimentology*, **55**, 869–898.

Desbarats, A.J. (1987) Numerical estimation of effective permeability in sand-shale formations. *Water Resour. Res.*, **23**, 273–286.

Deutsch, C. (1989) Calculating effective absolute permeability in sandstone/shale sequences. *SPE Form. Eval.*, **4**, 343–348.

Dickinson, W.R. (1970) Interpreting detrital modes of graywacke and arkose. *J. Sed. Res.*, **40**, 695–707.

Dickinson, W.R. (1985) Interpreting provenance relations from detrital modes of sandstones. In: *Provenance of Arenites* (Ed. Zuffa, G.G.), NATO ASI Series, Vol **148**, pp. 333–361. Springer, Dordrecht.

Dickinson, W.R., **Beard, L.S.**, **Brakenridge, G.R.**, **Erjavec, J.**, **Ferguson, R.**, **Inman, K.**, **Knepp, R.**, **Lindberg, F.A.** and **Ryberg, P.** (1983) Provenance of north American phanerozoic sandstones in relation to tectonic setting. *Geol. Soc. Am. Bull.*, **94**, 222–235.

Dmitrieva, E., **Jackson, C.A.L.**, **Huuse, M.** and **Kane, I.A.** (2018) Regional distribution and controls on the development of post-rift turbidite systems: insights from the Paleocene of the eastern North Viking graben, offshore Norway. *Pet. Geol. Conf. Proc.*, **8**, 147–170.

Dodd, T.J.H., **McCarthy, D.J.** and **Richards, P.C.** (2019) A depositional model for deep-lacustrine, partially confined, turbidite fans: early cretaceous, North Falkland Basin. *Sedimentology*, **66**, 53–80.

Dowey, P.J., **Hodgson, D.M.** and **Worden, R.H.** (2012) Pre-requisites, processes, and prediction of chlorite grain coatings in petroleum reservoirs: a review of subsurface examples. *Mar. Pet. Geol.*, **32**, 63–75.

Du Fornel, E., **Joseph, P.**, **Desaubliaux, G.**, **Eschard, R.**, **Guillocheau, F.**, **Lerat, O.**, **Muller, C.**, **Ravenner, C.** and **Sztrakos, K.** (2004) The southern Grès d'Annot outcrops (French Alps): an attempt at regional correlation. *Geol. Soc. London Spec. Publ.*, **221**, 137–160.

Edwards, D.A. (1991) Turbidity Current Dynamics, Deposits and Reversals. Doctoral Dissertation, University of Leeds, Leeds.

Edwards, D.A., **Leeder, M.R.**, **Best, J.L.** and **Pantin, H.M.** (1994) On experimental reflected density currents and the interpretation of certain turbidites. *Sedimentology*, **41**, 437–461.

Eggenhuisen, J.T., **Cartigny, M.J.B.** and **De Leeuw, J.** (2017) Physical theory for near-bed turbulent particle suspension capacity. *Earth Surf. Dyn.*, **5**, 269–281.

Ehrenberg, S.N. (1993) Preservation of anomalously high porosity in deeply buried sandstones by grain-coating chlorite: examples from the Norwegian continental shelf. *Am. Assoc. Pet. Geol. Bull.*, **77**, 1260–1286.

Færseth, R.B. and **Lien, T.** (2002) Cretaceous evolution in the Norwegian Sea—a period characterized by tectonic quiescence. *Mar. Pet. Geol.*, **19**, 1005–1027.

Fildani, A., **Clark, J.**, **Covault, J.A.**, **Power, B.**, **Romans, B.W.** and **Aiello, I.W.** (2018) Muddy sand and sandy mud on the distal Mississippi fan: implications for lobe depositional processes. *Geosphere*, **14**, 1051–1066.

Folk, R.L. and **Ward, W.C.** (1957) Brazos River bar [Texas]; a study in the significance of grain size parameters. *J. Sed. Res.*, **27**, 3–26.

Fonnesu, M., **Haughton, P.**, **Felletti, F.** and **McCaffrey, W.** (2015) Short length-scale variability of hybrid event beds and its applied significance. *Mar. Pet. Geol.*, **67**, 583–603.

Fonnesu, M., **Felletti, F.**, **Haughton, P.D.W.**, **Patacci, M.** and **McCaffrey, W.D.** (2018) Hybrid event bed character and distribution linked to turbidite system sub-environments: the north Apennine Gottero sandstone (north-West Italy). *Sedimentology*, **65**, 151–190.

Franzese, J.R. and **Spalletti, L.A.** (2001) Late triassic-early jurassic continental extension in SouthWestern Gondwana: tectonic segmentation and pre-break-up rifting. *J. S. Am. Earth Sci.*, **14**, 257–270.

Franzese, J. and **Spalletti, L.** (2003) Tectonic and paleoenvironmental evolution of Mesozoic sedimentary basins along the Andean foothills of Argentina (32°–54°S). *J. S. Am. Earth Sci.*, **16**, 81–90.

Franzese, J.R., **Veiga, G.D.**, **Schwarz, E.** and **Gómez-Pérez, I.** (2006) Tectonostratigraphic evolution of a Mesozoic graben border system: the Chachil depocentre, southern Neuquén Basin, Argentina. *J. Geol. Soc. London*, **163**, 707–721.

Gabrielsen, R.H., **Kyrkjebø, R.**, **Faleide, J.I.**, **Fjeldskaar, W.** and **Kjennerud, T.** (2001) The cretaceous post-rift basin configuration of the northern North Sea. *Pet. Geosci.*, **7**, 137–154.

Gazzi, P. (1966) Le arenarie del flysch sopracretaceo dell'Appennino modenese; Correlazioni coni flysch di Monghidoro. *Min. Petrogr Acta*, **12**, 69–97.

Grundvåg, S.A., **Johannessen, E.P.**, **Helland-Hansen, W.** and **Plink-Björklund, P.** (2014) Depositional architecture and evolution of progradationally stacked lobe complexes in the Eocene Central Basin of Spitsbergen. *Sedimentology*, **61**, 535–569.

Hampton, M.A. (1970) *Subaqueous Debris Flow and Generation of Turbidity Currents*. Stanford University, Stanford.

Hansen, L.A.S., **Hodgson, D.M.**, **Pontén, A.**, **Bell, D.** and **Flint, S.** (2019) Quantification of basin-floor fan pinchouts: examples from the Karoo Basin, South Africa. *Front. Earth Sci.*, **7**, 1–20.

Hansen, L.A.S., **Hodgson, D.M.**, **Pontén, A.**, **Thrana, C.** and **Latre, O.A.** (2021) Mixed axial and transverse deep-water systems: the cretaceous post-rift lysing formation, Offshore Norway. *Basin Res.*, **33**, 2229–2251.

Haughton, P.D.W., **Barker, S.P.** and **McCaffrey, W.D.** (2003) "Linked" debrites in sand-rich turbidite systems—origin and significance. *Sedimentology*, **50**, 459–482.

Haughton, P., **Davis, C.**, **McCaffrey, W.** and **Barker, S.** (2009) Hybrid sediment gravity flow deposits—classification, origin and significance. *Mar. Pet. Geol.*, **26**, 1900–1918.

Hay, D.C. (2012) Stratigraphic evolution of a tortuous corridor from the stepped slope of Angola. *Appl. Princ. Seism. Geomorphol. to Cont. Base-of-Slope Syst. Case Stud. from Seafloor Near-Seafloor Analog.*, 163–180.

Heald, M.T. and **Larese, R.E.** (1974) Influence of coatings on quartz cementation. *J. Sed. Res.*, **44**, 1269–1274.

Henstra, G.A., **Grundvåg, S.A.**, **Johannessen, E.P.**, **Kristensen, T.B.**, **Midtkandal, I.**, **Nystuen, J.P.**, **Rotevatn, A.**, **Surlyk, F.**, **Sæther, T.** and **Windelstad, J.** (2016) Depositional processes and stratigraphic architecture within a coarse-grained rift-margin turbidite system: the Wollaston Forland group, East Greenland. *Mar. Pet. Geol.*, **76**, 187–209.

Hiscott, R.N. (1994a) Loss of capacity, not competence, as the fundamental process governing deposition from turbidity currents. *J. Sed. Res.*, **64**, 209–214.

Hiscott, R.N. (1994b) Traction-carpet stratification in turbidites; fact or fiction? *J. Sed. Res.*, **64**, 204–208.

Hodgson, D.M. (2009) Distribution and origin of hybrid beds in sand-rich submarine fans of the Tanqua depocentre, Karoo Basin, South Africa. *Mar. Pet. Geol.*, **26**, 1940–1956.

Hodgson, D.M., **Flint, S.S.**, **Hodgetts, D.**, **Drinkwater, N.J.**, **Johannessen, E.P.** and **Luthi, S.M.** (2006) Stratigraphic evolution of fine-grained submarine fan systems, Tanqua depocenter, Karoo Basin, South Africa. *J. Sed. Res.*, **76**, 20–40.

Hodgson, D.M., **Kane, I.A.**, **Flint, S.S.**, **Brunt, R.L.** and **Ortiz-Karpf, A.** (2016) Time-transgressive confinement on the slope and the progradation of basin-floor fans: implications for the sequence stratigraphy of deep-water deposits. *J. Sed. Res.*, **86**, 73–86.

Hodgson, D.M., **Brooks, H.L.**, **Ortiz-Karpf, A.**, **Spychala, Y.**, **Lee, D.R.** and **Jackson, C.A.L.** (2019) Entrainment and abrasion of megaclasts during submarine landsliding and their impact on flow behaviour. *Geol. Soc. Spec. Publ.*, **477**, 223–240.

Howell, J.A., **Swcharz, E.**, **Spalletti, L.A.** and **Veiga, G.D.** (2005) The Neuquén Basin, Argentina: a case study in sequence stratigraphy and basin dynamics. *Geol. Soc. London Spec. Publ.*, **252**, 1–14.

Hulka, C. and **Heubeck, C.** (2010) Composition and provenance history of late cenozoic sediments in southeastern boliva: implications for Chaco foreland basin evolution and Andean uplift. *J. Sed. Res.*, **80**, 288–299.

Hurst, A., **Cartwright, J.A.**, **Duranti, D.**, **Huuse, M.** and **Nelson, M.** (2005) Sand injectites: an emerging global play in deep-water clastic environments. *Geol. Soc. London Pet. Geol. Conf. Ser.*, **6**, 133–144.

Hurst, A., **Cartwright, J.** and **Cartwright, J.A.** (2008) Sand injectites: implications for hydrocarbon exploration and production. *AAPG Mem.*, **87**, 34–49.

Hurst, A., **Scott, A.** and **Vigorito, M.** (2011) Physical characteristics of sand injectites. *Earth-Sci. Rev.*, **106**, 215–246.

Hussain, A., **Haughton, P.D.W.**, **Shannon, P.M.**, **Turner, J.N.**, **Pierce, C.S.**, **Obradors-Latre, A.**, **Barker, S.P.** and **Martinsen, O.J.** (2020) High-resolution X-ray fluorescence profiling of hybrid event beds: implications for sediment gravity flow behaviour and deposit structure. *Sedimentology*, **67**, 2850–2882.

Ingersoll, R.V. and **Suczek, C.** (1979) Petrology and provenance of Neogene sand from Nicobar and Bengal fans, DSDP sites 211 and 218. *J. Sediment. Petrol.*, **49**, 1217–1228.

Jackson, C.A.L., **Barber, G.P.** and **Martinsen, O.J.** (2008) Submarine slope morphology as a control on the development of sand-rich turbidite depositional systems: 3D seismic analysis of the Kyrre Fm (upper cretaceous), Måløy slope, offshore Norway. *Mar. Pet. Geol.*, **25**, 663–680.

Kane, I.A. and **Pontén, A.S.M.** (2012) Submarine transitional flow deposits in the Paleogene Gulf of Mexico. *Geology*, **40**, 1119–1122.

Kane, I.A., **Pontén, A.S.M.**, **Vangdal, B.**, **Eggenhuisen, J.T.**, **Hodgson, D.M.** and **Spychala, Y.T.** (2017) The stratigraphic record and processes of turbidity current transformation across deep-marine lobes. *Sedimentology*, **64**, 1236–1273.

Kneller, B. (1995) Beyond the turbidite paradigm: physical models for deposition of turbidites and their implications for reservoir prediction. *Geol. Soc. Spec. Publ.*, **94**, 31–49.

Kneller, B.C. and **Branney, M.J.** (1995) Sustained high-density turbidity currents and the deposition of thick massive sands. *Sedimentology*, **42**, 607–616.

Kneller, B.C. and **McCaffrey, W.D.** (1999) Depositional effects of flow nonuniformity and stratification within turbidity currents approaching a bounding slope: deflection, reflection, and facies variation. *J. Sed. Res.*, **69**, 980–991.

Kneller, B.C. and **McCaffrey, W.D.** (2003) The interpretation of vertical sequences in turbidite beds: the influence of longitudinal flow structure. *J. Sed. Res.*, **73**, 706–713.

Kneller, B., **Edwards, D.**, **McCaffrey, W.** and **Moore, R.** (1991) Oblique reflection of turbidity currents. *Geology*, **19**, 250–252.

Kuenen, P.H. (1951) Properties of turbidity currents of high density. *SEPM Spec. Publ.*, 14–33.

Leanza, H.A., **Mazzini, A.**, **Corfu, F.**, **Llambías, E.J.**, **Svensen, H.**, **Planke, S.** and **Galland, O.** (2013) The Chachil limestone (Pliensbachian-earliest Toarcian) Neuquén Basin, Argentina: U-Pb age calibration and its significance on the early Jurassic evolution of southwestern Gondwana. *J. S. Am. Earth Sci.*, **42**, 171–185.

Legarreta, L. and **Uliana, M.A.** (1996) The Jurassic succession in west-Central Argentina: stratal patterns, sequences and paleogeographic evolution. *Palaeogeogr. Palaeoclimatol. Palaeoecol.*, **120**, 303–330.

Leppard, C.W. and **Gawthorpe, R.L.** (2006) Sedimentology of rift climax deep water systems; lower Rudeis formation, hammam Faraun fault block, Suez rift, Egypt. *Sed. Geol.*, **191**, 67–87.

Lowe, D.R. (1982) Sediment gravity flows; II, depositional models with special reference to the deposits of high-density turbidity currents. *J. Sed. Res.*, **52**, 279–297.

Lowe, D.R. and **Guy, M.** (2000) Slurry-flow deposits in the Britannia formation (lower cretaceous), North Sea: a new perspective on the turbidity current and debris flow problem. *Sedimentology*, **47**, 31–70.

Marini, M., **Milli, S.**, **Ravnås, R.** and **Moscatelli, M.** (2015) A comparative study of confined vs. semi-confined turbidite lobes from the lower Messinian Laga Basin (central

Apennines, Italy): implications for assessment of reservoir architecture. *Mar. Pet. Geol.*, **63**, 142–165.

Marr, J.G., **Shanmugam, G.** and **Parker, G.** (2001) Experiments on subaqueous sandy gravity flows: the role of clay and water content in flow dynamics and depositional structures. *Bull. Geol. Soc. Am.*, **113**, 1377–1386.

Martínez-Doñate, A., **Privat, A.M.L.J.**, **Hodgson, D.M.**, **Jackson, C.A.L.**, **Kane, I.A.**, **Spychala, Y.T.**, **Duller, R.A.**, **Stevenson, C.**, **Keavney, E.**, **Schwarz, E.** and **Flint, S.S.** (2021) Substrate entrainment, depositional relief, and sediment capture: impact of a submarine landslide on flow process and sediment supply. *Front. Earth Sci.*, **9**, 1–23.

McArthur, A.D., **Hartley, A.J.**, **Archer, S.G.**, **Jolley, D.W.** and **Lawrence, H.M.** (2016) Spatiotemporal relationships of deep-marine, axial, and transverse depositional systems fromthe synrift upper Jurassic of the Central North Sea. *Am. Assoc. Pet. Geol. Bull.*, **100**, 1469–1500.

McCaffrey, W. and **Kneller, B.** (2001) Process controls on the development of stratigraphic trap potential on the margins of confined turbidite systems and aids to reservoir evaluation. *Am. Assoc. Pet. Geol. Bull.*, **85**, 971–988.

Middleton, G.V. and **Hampton, M.** (1973) Sediment gravity flows: mechanics of flow and deposition. In: *Turbidity and Deep Water Sedimentation* (Eds Middleton, G.V. and Bouma, A.H.), *SEPM, Pacificc Section, Short Course Lecture Notes*, 1–38. Available at: https://archives.datapages.com/data/pac_sepm/015/015001/pdfs/1.htm

Middleton, G.V. and **Neal, W.J.** (1989) Experiments on the thickness of beds deposited by turbidity currents. *J. Sed. Petrol.*, **59**, 297–307.

Mohrig, D., **Whipple, K.X.**, **Hondzo, M.**, **Ellis, C.** and **Parker, G.** (1998) Hydroplaning of subaqueous debris flows. *Bull. Geol. Soc. Am.*, **110**, 387–394.

Monnier, D., **Imbert, P.**, **Gay, A.**, **Mourgues, R.** and **Lopez, M.** (2014) Pliocene sand injectites from a submarine lobe fringe during hydrocarbon migration and salt diapirism: a seismic example from the lower Congo Basin. *Geofluids*, **14**, 1–19.

Mueller, P., **Patacci, M.** and **Di Giulio, A.** (2021) Hybrid event bed distribution in a mixed siliciclastic-calcareous turbidite succession: a cross-current perspective from the Bordighera sandstone, Ligurian Alps, NW Italy. *Ital. J. Geosci.*, **140**, 255–274.

Mulder, T. and **Alexander, J.** (2001) The physical character of subaqueous sedimentary density flow and their deposits. *Sedimentology*, **48**, 269–299.

Mutti, E. (1977) Distinctive thin-bedded turbidite facies and related depositional environments in the Eocene Hecho group (south-Central Pyrenees, Spain). *Sedimentology*, **24**, 107–131.

Mutti, E. (1979) Turbidites et cones sous-margins profonds. *Srdimentation Detrique (Fluviatile, Littorale Mar.*), 353–419.

Mutti, E. (1992) Turbidite Sandstones. 275.

Mutti, E. and **Ghibaudo, G.** (1972) Un esempio di torbiditi di conoide sottomarina esterna: Le Arenarie di San Salvatore (Formazione di Bobbio, Miocene) nell'Appennino di Piacenza. *Mem. Della'Accademia Delle Sci. di Torino, Cl. di Sci. Fis. Math. e Nat.*, **4**, 40.

Mutti, E. and **Ricci Lucchi, F.** (1972) Le torbiditi dell' Appennino settentrionale: introduzione all' analisi di facies. *Soc. Geol. Ital. Mem.*, **11**, 161–199.

Mutti, E. and **Sonnino, M.** (1981) Compensation cycles: a diagnostic feature of turbidite sandstone lobes. In: *International Association of Sedimentologists—European Regional Meeting*, pp. 120–123. Availabe at: http://pascal-francis.inist.fr/vibad/index.php?action=getRecordDetail&idt=9598738

Muzzi Magalhaes, P. and **Tinterri, R.** (2010) Stratigraphy and depositional setting of slurry and contained (reflected) beds in the Marnosoarenacea formation (LanghianSerravallian) northern Apennines, Italy. *Sedimentology*, **57**, 1685–1720.

Normark, W.R. (1970) Growth patterns of deep-sea fans. *Am. Assoc. Pet. Geol. Bull.*, **54**, 2170–2195.

Normark, W.R. (1978) Fan valleys, channels, and depositional lobes on modern submarine fans: characters for recognition of Sandy turbidite environments. *Am. Assoc. Pet. Geol. Bull.*, **62**, 912–931.

Pantin, H.M. and **Leeder, M.R.** (1987) Reverse flow in turbidity currents: the role of internal solitons. *Sedimentology*, **34**, 1143–1155.

Patacci, M., **Haughton, P.D.W.** and **McCaffrey, W.D.** (2014) Rheological complexity in sediment gravity flows forced to decelerate against a confining slope, Braux, SE France. *J. Sed. Res.*, **84**, 270–277.

Paull, C.K., **Talling, P.J.**, **Maier, K.L.**, **Parsons, D.**, **Xu, J.**, **Caress, D.W.**, **Gwiazda, R.**, **Lundsten, E.M.**, **Anderson, K.**, **Barry, J.P.**, **Chaffey, M.**, **O'Reilly, T.**, **Rosenberger, K.J.**, **Gales, J.A.**, **Kieft, B.**, **McGann, M.**, **Simmons, S.M.**, **McCann, M.**, **Sumner, E.J.**, **Clare, M.A.** and **Cartigny, M.J.** (2018) Powerful turbidity currents driven by dense basal layers. *Nat. Commun.*, **9**, 1–9.

Peakall, J., **McCaffrey, B.** and **Kneller, B.** (2000) A process model for the evolution, morphology, and architecture of sinuous submarine channels. *J. Sed. Res.*, **70**, 434–448.

Peakall, J., **Best, J.**, **Baas, J.H.**, **Hodgson, D.M.**, **Clare, M.A.**, **Talling, P.J.**, **Dorrell, R.M.** and **Lee, D.R.** (2020) An integrated process-based model of flutes and tool marks in deep-water environments: implications for palaeohydraulics, the Bouma sequence and hybrid event beds. *Sedimentology*, **67**, 1601–1666.

Pettijohn, F.J., **Potter, P.E.** and **Siever, R.** (1972) Petrographic classification and glossary. In: *Sand and Sandstone. Springer Study Edition*, p. 512. Springer Science & Business Media, New York, NY.

Pickering, K.T. and **Hilton, V.C.** (1998) *Turbidite Systems of Southeast France: Application to Hydrocarbon Prospectivity*. London: Vallis Press.

Pope, E.L., **Cartigny, M.J.**, **Clare, M.A.**, **Talling, P.J.**, **Lintern, D.G.**, **Vellinga, A.**, **Hage, S.**, **Açikalin, S.**, **Bailey, L.**, **Chapplow, N.**, **Chen, Y.**, **Eggenhuisen, J.T.**, **Hendry, A.**, **Heerema, C.J.**, **Heijnen, M.S.**, **Hubbard, S.M.**, **Hunt, J.E.**, **McGhee, C.**, **Parsons, D.R.**, **Simmons, S.M.**, **Stacey, C.D.** and **Vendettuoli, D.** (2022) First source-to-sink monitoring shows dense head controls sediment flux and runout in turbidity currents. *Sci. Adv.*, **8**, eabj3220.

Porten, K.W., **Kane, I.A.**, **Warchoł, M.J.** and **Southern, S.J.** (2016) A sedimentological process-based approach to depositional reservoir quality of deep-marine sandstones: an example from the springar formation, northwestern Vøring Basin, Norwegian Sea. *J. Sed. Res.*, **86**, 1269–1286.

Prélat, A. and **Hodgson, D.M.** (2013) The full range of turbidite bed thickness patterns in submarine lobes: controls and implications. *J. Geol. Soc. London*, **170**, 209–214.

Prélat, A., **Hodgson, D.M.** and **Flint, S.S.** (2009) Evolution, architecture and hierarchy of distributary deep-water deposits: a high-resolution outcrop investigation from the Permian Karoo Basin, South Africa. *Sedimentology*, **56**, 2132–2154.

Privat, A.M.L.J. (2019) Sedimentology and tectono-stratigraphic development of the syn-to post-rift transition in Southern Neuquen Basin (Argentina) and controls on early post-rift submarine lobes of the Los Molles Formation. Doctoral dissertation, University of Leeds, Leeds.

Privat, A.M.J., **Hodgson, D.M.**, **Jackson, C.A.**, **Schwarz, E.** and **Peakall, J.** (2021) Evolution from syn-rift carbonates to early post-rift deep-marine intraslope lobes: the role of rift basin physiography on sedimentation patterns. *Sedimentology*, **68**, 2563–2605.

Prosser, S. (1993) Rift-related linked depositional systems and their seismic expression. *Geol. Soc. Spec. Publ.*, **71**, 35–66.

Ravnås, R. and **Steel, R.J.** (1998) Architecture of marine rift-basin successions. *Am. Assoc. Pet. Geol. Bull.*, **82**, 110–146.

Ross, W.C., **Halliwell, B.A.**, **May, J.A.**, **Watts, D.E.** and **Syvitski, J.P.M.** (1994) Slope readjustment: a new model for the development of submarine fans and aprons. *Geology*, **22**, 511–514.

Scott, A., **Hurst, A.** and **Vigorito, M.** (2013) Outcrop-based reservoir characterization of a kilometer-scale sand-injectite complex. *Am. Assoc. Pet. Geol. Bull.*, **97**, 309–343.

Sequeiros, O.E. (2012) Estimating turbidity current conditions from channel morphology: a Froude number approach. *J. Geophys. Res. Ocean.*, **117**, 1–19.

Sequeiros, O.E., **Naruse, H.**, **Endo, N.**, **Garcia, M.H.** and **Parker, G.** (2009) Experimental study on self-accelerating turbidity currents. *J. Geophys. Res. Ocean.*, **114**, 1–26.

Sequeiros, O.E., **Mosquera, R.** and **Pedocchi, F.** (2018) Internal structure of a self-accelerating turbidity current. *J. Geophys. Res. Ocean.*, **123**, 6260–6276.

Shanmugam, G. and **Moiola, R.J.** (1988) Submarine fans: characteristics, models, classification, and reservoir potential. *Earth Sci. Rev.*, **24**, 383–428.

Sinclair, H.D. (2000) Delta-fed turbidites infilling topographically complex basins: a new depositional model for the annot sandstones, SE France. *J. Sed. Res.*, **70**, 504–519.

Sinclair, H.D. and **Tomasso, M.** (2002) Depositional evolution of confined turbidite basins. *J. Sed. Res.*, **72**, 451–456.

Smith, R. (2004) Turbidite systems influenced by structurally induced topography in the multi-sourced Welsh Basin. *Geol. Soc. Spec. Publ.*, **222**, 209–228.

Smith, R. and **Joseph, P.** (2004) Onlap stratal architectures in the Grès d'Annot: geometric models and controlling factors. *Geol. Soc. Spec. Publ.*, **221**, 389–399.

Sohn, Y.K. (1997) On traction-carpet sedimentation. *J. Sed. Res.*, **67**, 502–509.

Sohn, Y.K., **Choe, M.Y.** and **Jo, H.R.** (2002) Transition from debris flow to hyperconcentrated flow in a submarine channel (the cretaceous cerro Toro formation, southern Chile). *Terra*, **14**, 405–415.

Sømme, T.O., **Helland-hansen, W.**, **Martinsen, J.** and **Thurmond, J.B.** (2009) Relationships between morphological and sedimentological parameters in source-to-sink systems: a basis for predicting semi-quantitative characteristics in subsurface systems. *Basin Res.*, **21**, 361–387.

Southern, S.J., **Patacci, M.**, **Felletti, F.** and **McCaffrey, W.D.** (2015) Influence of flow containment and substrate entrainment upon sandy hybrid event beds containing a co-genetic mud-clast-rich division. *Sediment. Geol.*, **321**, 105–122.

Southern, S.J., **Kane, I.A.**, **Warchoł, M.J.**, **Porten, K.W.** and **McCaffrey, W.D.** (2017) Hybrid event beds dominated by transitional-flow facies: character, distribution and significance in the maastrichtian springar formation, north-west vøring basin. *Norwegian Sea*, **64**, 747–776.

Soutter, E.L., **Kane, I.A.**, **Fuhrmann, A.**, **Cumberpatch, Z.A.** and **Huuse, M.** (2019) The stratigraphic evolution of onlap in siliciclastic deep-water systems: autogenic modulation of allogenic signals. *J. Sed. Res.*, **89**, 890–917.

Soutter, E.L., **Bell, D.**, **Cumberpatch, Z.A.**, **Ferguson, R.A.**, **Spychala, Y.T.**, **Kane, I.A.** and **Eggenhuisen, J.T.** (2021) The influence of confining topography orientation on experimental turbidity currents and geological implications. *Front. Earth Sci.*, **8**, 540633. https://doi.org/10.3389/feart.2020.540633.

Spychala, Y.T., **Hodgson, D.M.**, **Flint, S.S.** and **Mountney, N.P.** (2015) Constraining the sedimentology and stratigraphy of submarine intraslope lobe deposits using exhumed examples from the Karoo Basin, South Africa. *Sediment. Geol.*, **322**, 67–81.

Spychala, Y., **Hodgson, D.** and **Lee, D.** (2017a) Autogenic controls on hybrid bed distribution in submarine lobe complexes. *Mar. Pet. Geol.*, **88**, 1078–1093.

Spychala, Y.T., **Hodgson, D.M.**, **Stevenson, C.** and **Flint, S.S.** (2017b) Aggradational lobe fringes: the influence of subtle intrabasinal seabed topography on sediment gravity flow processes and lobe stacking patterns. *Sedimentology*, **64**, 582–608.

Stevenson, C.J., **Jackson, C.A.L.**, **Hodgson, D.M.**, **Hubbard, S.M.** and **Eggenhuisen, J.T.** (2015) Deep-water sediment bypass. *J. Sed. Res.*, **85**, 1058–1081.

Stevenson, C.J., **Peakall, J.**, **Hodgson, D.M.**, **Bell, D.** and **Privat, A.** (2020) Tb or not tb: banding in turbidite sandstones. *J. Sed. Res.*, **90**, 821–842.

Stow, D.A. (1985) Brae oilfield turbidite system, North Sea. In: *Submarine Fans and Related Turbidite Systems* (Eds Bouma, A.H., Normark, W.R. and Barnes, N.E.), pp. 231–236. Springer, York, NY.

Strachan, L.J., **Rarity, F.**, **Gawthorpe, R.L.**, **Wilson, P.**, **Sharp, I.** and **Hodgetts, D.** (2013) Submarine slope processes in rift-margin basins, Miocene Suez rift, Egypt. *Bull. Geol. Soc. Am.*, **125**, 109–127.

Sumner, E.J., **Amy, L.A.** and **Talling, P.J.** (2008) Deposit structure and processes of sand deposition from decelerating sediment suspensions. *J. Sed. Res.*, **78**, 529–547.

Sylvester, Z. and **Lowe, D.R.** (2004) Textural trends in turbidites and slurry beds from the Oligocene flysch of the East Carpathians, Romania. *Sedimentology*, **51**, 945–972.

Talling, P.J., **Peakall, J.**, **Sparks, R.S.J.**, **Cofaigh, C.Ó.**, **Dowdeswell, J.A.**, **Felix, M.**, **Wynn, R.B.**, **Baas, J.H.**, **Hogg, A.J.**, **Masson, D.G.**, **Taylor, J.** and **Weaver, P.P.E.** (2002) Experimental constraints on shear mixing rates and processes: implications for the dilution of submarine debris flows. *Geol. Soc. London Spec. Publ.*, **203**, 89–103.

Talling, P.J., **Amy, L.A.**, **Wynn, R.B.**, **Peakall, J.** and **Robinson, M.** (2004) Beds comprising debrite sandwiched within co-genetic turbidite: origin and widespread occurrence in distal depositional environments. *Sedimentology*, **51**, 163–194.

Talling, P.J., **Masson, D.G.**, **Sumner, E.J.** and **Malgesini, G.** (2012) Subaqueous sediment density flows: depositional processes and deposit types. *Sedimentology*, **59**, 1937–2003.

Terlaky, V. and **Arnott, R.W.C.** (2014) Matrix-rich and associated matrix-poor sandstones: avulsion splays in slope and basin-floor strata. *Sedimentology*, **61**, 1175–1197.

Terlaky, V. and **Arnott, R.W.C.** (2016) The control of terminal-splay sedimentation on depositional patterns and stratigraphic evolution in avulsion-dominated, unconfined, deep-marine basin-floor systems. *J. Sed. Res.*, **86**, 786–799.

Tinterri, R. (2011) Combined flow sedimentary structures and the genetic link between sigmoidal-and hummocky-cross stratification. *GeoActa*, **10**, 43–85.

Tinterri, R., **Muzzi Magalhaes, P.**, **Tagliaferri, A.** and **Cunha, R.S.** (2016) Convolute laminations and load structures in turbidites as indicators of flow reflections and decelerations against bounding slopes. Examples from the Marnoso-arenacea formation (northern Italy) and Annot sandstones (south eastern France). *Sed. Geol.*, **344**, 382–407.

Tőkés, L. and **Patacci, M.** (2018) Quantifying tabularity of turbidite beds and its relationship to the inferred degree of basin confinement. *Mar. Pet. Geol.*, **97**, 659–671.

Van der Plas, L. and **Tobi, A.C.** (1965) Reliability of point counting results; reply. *Am. J. Sci.*, **263**, 722–724.

Veiga, G.D., **Schwarz, E.**, **Spalletti, L.A.** and **Massaferro, J.L.** (2013) Anatomy and sequence architecture of the early post-rift In the Neuquen Basin (Argentina): a response to physiography and Relative Sea-level changes. *J. Sed. Res.*, **83**, 746–765.

Vergani, G.D., **Tankard, A.J.**, **Belotti, H.J.** and **Welsink, H.J.** (1995) Tectonic evolution and paleogeography of the Neuquén Basin, Argentina. *Pet. Basins S. Am.*, **1904**, 383–402.

Weaver, C. (1931) Paleontology of the Jurassic and Cretaceous of West Central Argentina. Memoir University of Washington 1.

Weaver, C. (1942) A general summary of the Mesozoic of south and Central America. *Proceedings of the eighth American scientific congress held in Washington May*, **10-18**, 149–193.

Winker, C.D. (1996) High-resolution seismic stratigraphy of a late Pleistocene submarine fan ponded by salt-withdrawal mini-basins on the Gulf of Mexico continental slope. *Proc. Annu. Offshore Technol. Conf.*, **1**, 619–622.

Zachariah, A.J., **Gawthorpe, R.**, **Dreyer, T.** and **Corfield, S.** (2009a) Controls on early post-rift physiography and stratigraphy, lower to mid-cretaceous, North Viking graben, Norwegian North Sea. *Basin Res.*, **21**, 189–208.

Zachariah, A.J., **Gawthorpe, R.L.** and **Dreyer, T.** (2009b) Evolution and strike variability of early post-rift deep-marine depositional systems: lower to mid-cretaceous, North Viking graben, Norwegian North Sea. *Sed. Geol.*, **220**, 60–76.

Zuffa, G.G. (1985) *Optical Analyses of Arenites: Influence of Methodology on Compositional Results. Proven. arenites*, pp. 165–189. Springer, Dordrecht.

Manuscript received 17 July 2022; revision accepted 23 January 2023

Supporting Information

Additional information may be found in the online version of this article:

Figure S1. Density plots of S1–S7B sample beds.
Figure S2. Density plots of S8–S15 sample beds.
Table S1. Mineralogy table of detrital grains of the analysed samples: Lithoclasts are subdivided into volcanic (Lv), metamorphic (Lm) and sedimentary (Ls) lithoclasts.
Table S2. Grain size table.